Study of waves and structures at the boundaries of magnetospheres

Stefanos Giagkiozis

Automatic Control and Systems Engineering

The University of Sheffield

A dissertation submitted in partial fulfilment of the requirements for the degree of

Doctor of Philosophy in

October 2018

Executive Summary

Plasma exists in abundance throughout the universe and governs a large number of astrophysical processes that have been observed and are of interest. Studying the interactions of plasma with magnetic field waves, magnetic dipoles and counter-streaming plasma flows can provide insight in the fundamental physics that govern the universe and its evolution.
In order to study these phenomena in-situ, we are limited to spacecraft measurements in the heliosphere. Planetary missions are the ones that provide the largest quantities of measurements of the same phenomenon, due to their orbital parameters. On the other hand, the cost of these missions, generally limits them to a single spacecraft with the exception of spacecraft that orbit the Earth.
This thesis is mainly concerned with the study of the interactions of plasma at the boundary of magnetic dipoles and the electromagnetic waves that are present in such environments. Upstream of the boundary between the Earth's magnetic field and the interplanetary magnetic field, the magnetopause (average distance from Earth $\sim 10R_E \sim 63000\,km$), a region of plasma heated by the bow shock exists, the magnetosheath. This region is rich in electromagnetic emissions and magnetic structures. The physical processes at the bow shock can provide insight in astrophysical phenomena. The interaction of the waves in the magnetosheath with the surrounding plasma is also of great interest as they govern the behaviour of the plasma.
Specifically this thesis initially examines the physical processes at the bow shocks of Earth and Venus. The magnetic environments of the two planets are different, as Venus does not have a magnetic field generated by the rotation of its core, unlike Earth. This means that there is benefit in studying both under the same framework in order to determine the underlying physics. The work then continuous with the examination of electromagnetic emissions downstream of the Earth's bow shock. These waves have been named lion roars and their exact origin is unclear, although they have been shown to change the properties of the plasma they interact with.

Acknowledgements

Firstly I would like to thank my supervisor, Michael Balikhin, for treating me like family.
I would like to thank Ifigeneia for the support and bearing with me during my studies.
I would also like to thank my brother and my family for keeping me in the right path.
I would like to thank my friends for helping me forget work.
Special thanks go to Simon Walker and Richard Boyton for tolerating me and my questions and the great times at AGU.

Statement of Originality

Unless otherwise stated in the text, the work described in this thesis was carried out solely by the candidate. None of this work has already been accepted for any other degree, nor is it being concurrently submitted in candidature for any degree.

Candidate: _____

Stefanos Giagkiozis

Supervisor: _____

Michael A. Balikhin

Supervisor: _____

Simon A. Pope

X

Contents

List of Figures

List of Tables

Chapter 1

Introduction

1.1 Plasma

Plasma is a gas that consists of equal number of positively and negatively charged particles. As the thermal energy of the molecules in gases increases, the bonds between the electrons and core of the molecules breaks and the electrons are freed. When enough energy is provided, a large number of free electrons and ions exists, so that the gas as a whole can be affected by electric and magnetic fields. Plasma can be categorised in collisionless and collisional plasma. Collisional plasma can be further categorised into fully and partially ionised plasma.

Plasma is quasinetural, which is to say that the positive charge is equal to the negative charge. It has been estimated that 99% of the visible matter in the universe is in the plasma state, which shows the importance of studying physical phenomena related to this state of matter. Because of the vastly different locations where plasma can be found, the properties that characterise plasma have a very large range. Table 1.1 shows the typical densities and temperatures observed at different regions in space and phenomena [see Kallenrode, 2004]. In plasma physics the temperature is customarily measured in energetic units $k_B T$ expressed in electronvolts (eV), where k_B is Boltzmanns constant and T is the temperature in K. $1\,eV$ is the energy that an electron requires to move across a $1\,V$ electric potential. From the table it is clear that plasma can be found throughout the universe as well as in everyday objects and phenomena. To put the large range of temperatures and number densities of

Table 1.1: Typical plasma characteristics in some regions in space and phenomena.

Region/Phenomenon	Temperature $[eV]$	Number Density $[cm^{-3}]$
Solar Wind	$\sim 10^1$	$\sim 10^0$
Magnetoshpere	$\sim 10^{0.5}$	$\sim 10^4$
Fusion Reactor	$\sim 10^4$	$\sim 10^{17}$
Laser Plasma	$\sim 10^2$	$\sim 10^{21}$
Solar Corona	$\sim 10^2$	$\sim 10^9$

plasma into perspective, it is useful to consider that the highest melting point of a solid, under normal atmospheric pressure, is that of Tungsten at $\sim 0.318\,eV$ and a boiling point at $\sim 0.534\,eV$. For a gas of charged particles to be classified as plasma, three conditions must be met. In order to express them, we must first define some quantities.

The Debye length λ_D, is the distance at which the Coulomb potential of a charge is shielded by the collective particle polarisation. The Debye length is given by

$$\lambda_D = \left(\frac{\epsilon_0 k_B T_e}{n_e e^2}\right)^{1/2} \tag{1.1}$$

where T_e is the electron temperature, k_B is the Bolzmann constant, n_e is the electron density and e is the electron charge.

Inside the sphere with the radius of λ_D the number of particles is given by $\frac{4\pi}{3} n_e \lambda_D^3$, based on which the plasma parameter as $\Lambda = n_e \lambda_D^3$. This parameter determines how many particles are inside a Debye sphere, which in turn can be expressed in terms of the particle mean energy and the potential energy of the particle due to its nearest neighbour. The potential energy is proportional to $n_e^{1/3}$, which is inversely proportional to the distance between the average distance between particles.

The third condition relates to the average time between two particle collisions (τ_n) that occur inside the plasma as a function of the the plasma frequency. When the plasma is disturbed by an external source, the lighter electrons in the plasma oscillate around the heavier ions in an attempt to restore quasineutrality. The frequency of this oscilation is the plasma frequency and it is dependent upon the density of the plasma. Specifically, considering the electrons, the electron plasma frequency is

given by

$$\omega_{pe} = \left(\frac{4\pi n_e e^2}{m_e}\right)^{1/2} \tag{1.2}$$

The average collision time (τ_n) is important because when the plasma has a large number of neutral particles, the electrons will collide too often with the neutrals. This will lead to equilibrium of the electrons with the neutrals.

Based on the above, the three criteria that characterise plasma are the following

- $L \gg \lambda_D$ where L is the physical dimension of the system.
- $\Lambda \gg 1$
- $\omega_{pe}\tau_n \gg 1$

The last condition is more important for partially ionised plasmas and ensures that the plasma is not affected by neutral particles to a significant degree.

In contrast, space plasmas are not only fully ionised, but they are also collisionless in the majority of the cases. This means that the collision frequency between particles in general is not significant. In this types of plasmas, energy is transferred through wave-particle interactions and not binary particle collisions.

1.2 The Sun

Out Sun is the celestial body that allows life to occur on Earth, since it is what provides the energy for every organism on the planet. As our societies evolved through the millennia, they did so by improving the means and efficiency of storing this energy.

The solar wind that originates from the Sun has a typical velocity of $\sim 450\, km/sec$ in the vicinity of the Earth's orbit. This plasma interacts with the magnetic dipole, suppressing the dayside and elongating the nightside magnetosphere.

The anatomy of the Sun as summarised by the picture from NASA in Figure 1.1. Internally the Sun consists of the core, where the nuclear reactions take place and generate the energy we see as visible light. The radiative zone, is the region responsible for the transfer of energy. The convective zone, is the outer layer of the interior

and is in constant motion.

The atmosphere of the Sun is separated in the Photosphere, which is what we can see when looking at the Sun with our eyes. Above the photosphere, the Chromosphere is a region where the temperature is observed to rise from 6000 C° to 20000°. Finally a transition layer separates the chromosphere from the substantially hotter solar Corona.

The activity of the Sun is described based on features that we are able to detect, such as sun spots, solar flares and coronal mass ejections (CMEs). Sunspots, as the word describes, are black marks on the Suns photosphere, that have been measured to have a smaller temperature. The temperature difference is due to the increased magnetic flux that is observed on sunspots, that trap the material and they often appear in pairs of reverse magnetic polarity.

Solar flares are bursts of radiation from the Sun that are able to disrupt satellites orbiting the Earth as well as our atmosphere.

Finally CMEs are bursts of plasma that is released due to the reconnection of strong magnetic field lines that were containing this plasma. When a CME occurs, the material that is ejected can travel with a velocity of more than $\sim 1000\, km/sec$. As this high speed plasma comes with contact with the Earth, they can drive particles into the atmosphere through the poles which can even affect ground electric systems.

1.3 The Heliosphere

The heliosphere is a region of space we have defined as the dominion of the Sun. The plasma expelled by the Sum in an outwards direction, meets the interstellar medium at a point called the Heliopause. Between the Sun and the Heliopause we can find the termination shock. This is the boundary where the solar wind decelerates and in the Heliosheath, the region between the termination shock and the Heliopause, the solar wind is more dense and hot due to the interstellar wind. In the illustration in Figure 1.2, the locations of the Voyager 1 and 2 are outdated and in fact Voyager 1 is in the interstellar medium since August 25 2012, after it crossed

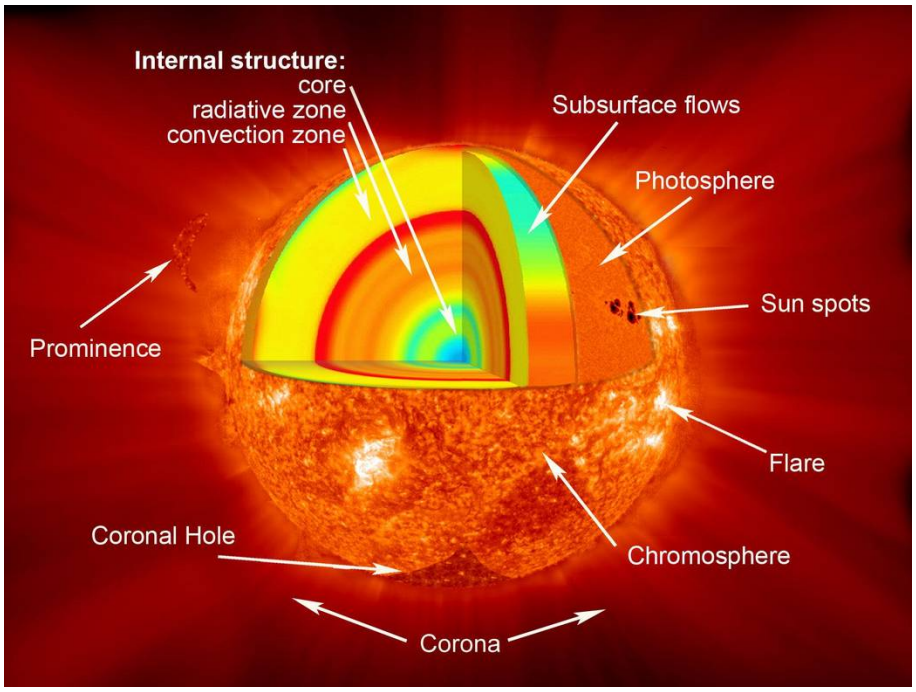

Figure 1.1: An image showing the various layers of the Sun downloaded from `https://www.nasa.gov/mission_pages/sunearth/science/Sunlayers.html`.

the Heliopause, while Voyager 2 is still inside the Heliosheath. Finally in the Figure 1.2 a bow shock is shown in front of the Heliopause. This bow shock was originally hypothesised to exist but a study conducted on IBEX measurements suggested that it does not exist McComas et al. [2012]. Inside the termination shock boundary, the solar wind interacts with the magnetic fields of the planets forming shocks, as well as interplanetary shocks from the different streams of plasma.

1.4 The Magnetosphere of the Earth

The Earth has a magnetic field which acts as an obstacle to the solar wind. Because of this a bow shock is formed in front of the Earth. The bow shock heats the incoming solar wind and slows down its speed. The shocked solar wind is then deflected around the magnetosphere, since it cannot penetrate it. The boundary that separates the interplanetary magnetic field, which originates from the Sun, and the magnetoshpere of the Earth, is the magnetopause.

The shape of the Earth's magnetosphere is not spherical, but its shape is distorted by

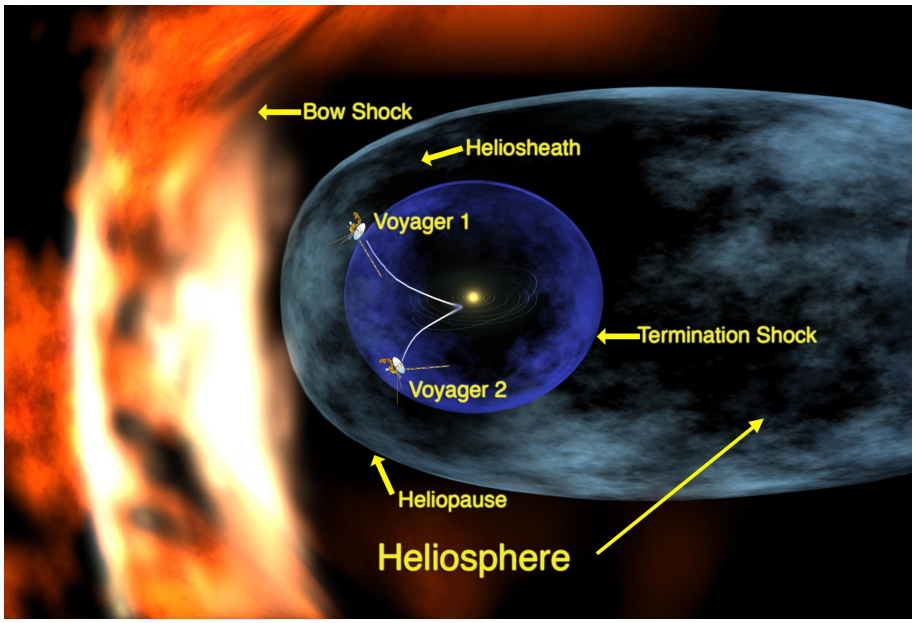

Figure 1.2: An artistic conception of the Heliosphere downloaded from `https://www.nasa.gov/mission_pages/sunearth/science/Heliosphere.html`.

the solar wind. Specifically on the day side, it is suppressed, while at the night side it is elongated. The plasma in the magnetosphere consists of plasma that originates from the solar wind and from the ionosphere. The solar wind plasma is introduced in the magnetosphere through the polar cusps.

The plasma in the magnetosphere is mainly concentrated in the radiation belts. The plasma in the radiation belts consists of energetic electrons and ions that move along the magnetic field lines and move between the two hemispheres in an oscillatory motion. The radiation belts are situated between 2 and 6 Earth radii and typical plasma density and temperature is $1\,cm^{-3}$ and $5 \cdot 10^7\,K$ respectively.

1.5 Outline

In Chapter 2 the theoretical background of the thesis is provided. The chapter intends to provide a build up towards the study of the next chapter with a focus on the definition of quantities that are of interest, while providing the reason why they are of interest.

In Chapter 3 a study on the velocity of collisionless shocks is provided. The impor-

tance of being able to estimate this quantity is highlighted and two methods for its estimation with a single spacecraft are examined. The accuracy of the methods is determined and an example usage on measurements from the Venusian bow shock is presented.

Chapter 4 is dedicated to a statistical study of electromagnetic emissions observed behind the Earth's bow shock.

Finally the conclusions of the study are presented in Chapter 5.

1.6 Contributions

The main contributions of this work are:

- Quantitative analysis of the accuracy of single spacecraft methods for the estimation of the velocity of collisionless shocks. This work was published in Journal of Geophysical Research : Space Physics [Giagkiozis et al., 2017] and Chapter 3 is based on this work.

- Application of the accuracy estimates of the single spacecraft methods on a Venusian bow shock crossing, which shows cases where the methods can be used to determine accurately the scales of the shock.

- Statistical examination of the properties of lion roars in the magnetosheath, using high sampling magnetic and electric field measurements. This work was published in Journal of Geophysical Research : Space Physics [Giagkiozis et al., 2018] and Chapter 4 is based on this work.

Chapter 2

Theoretical Background

2.1 Introduction

This thesis is partially focused on the study of collisonless shocks (CS). As briefly mentioned in Chapter 1 CS are ubiquitous throughout the universe. In the heliosphere they can be found in many locations, such as upstream of the Earth's magnetopause, in front of Venus, in the interplanetary space, the termination shock and others. The are named collisionless because t he energy dissipation across the shock is not the result of particle collisions, like in hydrodynamic shock. They occur in collisionless plasma and therefore other mechanisms are responsible for this energy conversion from kinetic energy to thermal.

Similarly to shock waves in ordinary gasses, CS increase the entropy of the incoming flow by converting the kinetic energy of the flow into thermal energy. In order to obtain a steady shock, a wave must steepen until it has a very small spatial scale, while a mechanism must dissipate the energy of the flow for the shock to remain formed and not break.

2.2 Magnetohydrodynamic Waves

The theory of magnetohydrodynamics (MHD) describes the evolution of macroscopic quantities in plasmas, by treating the plasma as a fluid. The position and velocity of the particles in a plasma are described by a distribution function. The evolution of this particle distribution function in a collisionless plasma is then described by

the Vlasov equation. By considering the plasma as a fluid, one can then derive the MHD equations that describe the evolution of the moments of the distribution function of the plasma, such as density, bulk flow velocity, pressure and temperature. The ideal MHD theory, consists of a system of equations for the conservation of mass, momentum and entropy, as well as Faraday's law and $\nabla \cdot \mathbf{B} = 0$. Finally, in the ideal MHD case, the magnetic field is considered to be frozen in the plasma. [Baumjohann et al., 1996; BELLAN, 2008]

Where the plasma is homogeneous and the magnetic field is constant, we can obtain, from the ideal MHD, a dispersion relation whose solutions correspond to three propagating elementary plasma waves. The phase speeds of these waves depend upon their propagation angle (θ_{kB}) relative to the background magnetic field (B) as well as two fundamental speeds in plasma. The sound speed (C_S) and the Alfvén speed (C_A) defined as

$$C_S = \sqrt{\frac{\gamma P}{\rho}} \tag{2.1}$$

$$C_A = \sqrt{\frac{B^2}{4\pi\rho}} \tag{2.2}$$

where γ is the specific heats ratio, P is the pressure and ρ is the density of the plasma.

Ordered based on their phase speed the three waves are named the *fast magnetosonic* (V_f), the *intermediate* (V_i) and the *slow* (V_s). The velocity of each defined as

$$V_i = [C_A^2 cos(\theta_{kB})^2]^{1/2} \tag{2.3}$$

$$V_{f,s} = \left(\frac{1}{2}\left[C_A^2 + C_S^2 \pm [(C_A^2 + C_S^2)^2 - 4C_A^2 C_S^2 cos(\theta_{kB})^2]^{1/2}\right]\right)^{1/2} \tag{2.4}$$

where the sign + (-) corresponds to fast (slow) magnetosonic flows.

All three waves depend on the propagation direction relative to the background magnetic field and the plasma beta ($\beta = \frac{8\pi p}{B^2}$) which defines the ratio of the thermal to magnetic pressure.

The intermediate wave does not propagate at $\theta_{kB} = 90°$ and at parallel propagation relative to the magnetic field its phase velocity is the Alfvén speed, and it is called the shear-Alfvén wave. As its propagation angle increases its phase velocity decreases.

The fast and the slow magnetosonic waves, unlike the intermediate wave, are both compressional waves, since they perturb the plasma density and pressure as they propagate. In the cold plasma limit, where the plasma thermal energy tends to 0, or β tends to zero, the slow wave does not propagate, while the fast wave propagates at the Alfvén speed.

Figure 2.1 shows the phase speeds of the three plasma waves relative to their propagation direction for four different $\frac{C_S}{C_A}$ cases. The C_A and C_S are also included for reference. When $\beta < 1$, lower plasma temperature, the sound velocity is smaller than the Alfvén speed. In this case for $\theta_{kB} = 0°$, the intermediate and the fast magnetosonic waves have the same velocity, the Alfvén speed. As β increases, the speed of sound increases , the intermediate and the slow wave phase velocities begin to look similar, but they are equal only at $\theta_{kB} = 0°$. For $C_S > C_A$ and propagation angle $\theta_{kB} = 0°$ the fast wave has $V_f = C_S$.

Both the sound and Alfvén velocities, in other words pressure and magnetic energy fluctuations, contribute to the fast magnetosonic wave, while for the slow wave they oppose each other.

A summary of the wave properties of the three distinct MHD waves [Kantrowitz and Petschek, 1964] is that

- The fast and the slow waves modify the magnitude of the tangential magnetic field component, since they are coplanar to the background magnetic field and the wave normal. The intermediate wave rotates the tangential magnetic field component, but doesn't change its magnitude, since it is a purely transverse wave and the changes are perpendicular to the background magnetic field.

- For the fast mode, as the density increases, the magnetic pressure increases. For the slow wave as the density decreases, the magnetic pressure increases.

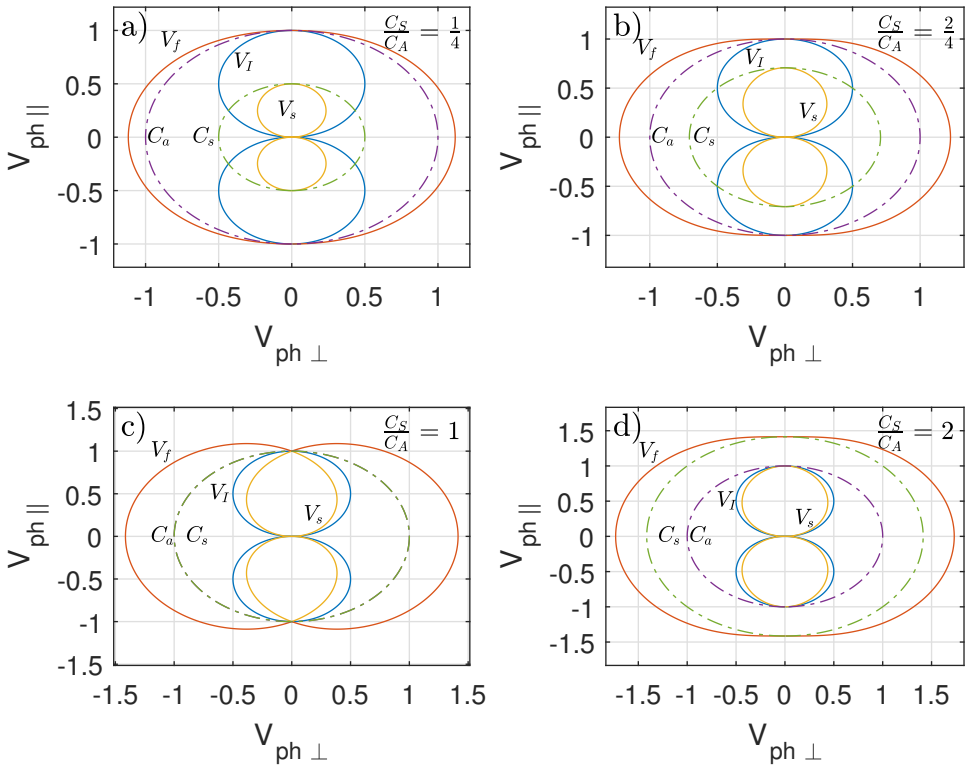

Figure 2.1: Phase velocity of the elementary plasma waves plotted for different $\frac{C_S}{C_A}$ ratios. The Alfvén (purple dashed line) and sound (green dashed line) speeds are also plotted for reference. The orange, blue and yellow lines correspond to the fast, intermediate and slow waves respectively.

The intermediate wave does not change the magnetic or thermal pressure.

Because the slow and fast MHD waves are compressional, they can steepen and form a discontinuity [Kantrowitz and Petschek, 1964]. In the special case where the waves propagate with $\theta_{kB} = 0$, the slow wave can steepen for low β and the fast wave for high β. [Hada and Kennel, 1985] calculated the parameters for which the two waves will steepen, by calculating the damping rates of the waves from kinetic theory. They concluded that fast waves will always steepen, while slow waves should rarely steepen at 1 AU, unless the plasma is characterised by low ion β.

2.3 MHD Shocks

When sufficient dissipation can be provided, these compressional waves can form steady shocks. While MHD theory cannot provide information about the dissipation

processes, they can provide information on the relationship between the upstream and downstream regions of the shock. The upstream regions is the un-shocked region and the downstream region is the shocked. The shock front separates the upstream and downstream region. The steepest part of the magnetic field magnitude of the shock front is called the *ramp*.

The relationship between the upstream and the downstream regions across MHD shocks [De Hoffmann and Teller, 1950], can be described by the Rankine-Hugionion (RH) jump conditions [see Baumjohann and Treumann, 1996] and are categorised in slow, fast shocks [see Kennel et al., 1985; Balogh and Riley, 1997].

The fast shock is characterised by an upstream bulk flow velocity V_b higher than V_f and are the most commonly observed shocks, while downstream of the shock $V_f > V_b > V_i$.

Slow shocks have been very rarely identified in solar wind observations [see e.g. Whang et al., 1996]. They are characterised by a low plasma β and their structure strongly depends on it. Slow shocks are shocks were $V_i > V_b > V_s$ and downstream $V_b < V_s$.

Rotational discontinuities are characterised by more than one combination of upstream to downstream bulk flow velocity transitions. According to Balogh and Riley [1997] the existence of intermediate shocks has been argued and their properties unclear. Observations of intermediate shocks have not been verified as the evidence of intermediate shock observations can also be interpreted as observations of rotational discontinuities. The majority of evidence of their existence has been based on the results of simulations and analytical work [Wu, 1987; Wu and Hada, 1991; Hada, 1994].

2.3.1 Shock Propagation Direction

The RH relations define a planar and stationary shock front. They express the changes that occur across the shock in the normal direction to that shock front. In order to define such a frame of reference the vector normal to the shock front ($\mathbf{n}$) needs to be defined. The shock is assumed to be propagating parallel to this vector

and in this direction $\nabla \cdot (\mathbf{B} \cdot \mathbf{n}) = 0$, derived from Maxwell's equations.
The propagation angle relative to the background magnetic field (θ_{Bn}) is one of the parameters that characterise CS and play an important role on their structure. When $\theta_{Bn} < 45°$ the shock is said to be quasi-parallel and when $\theta_{kB} > 45°$ the shock is quasi-perpendicular. This separation is made because in perpendicular shocks, the reflected particles are turned around by the magnetic field, due to the geometry, while in parallel shocks they can stream freely to infinity, for the same reason. This is a very important shock parameter and it will be used throughout this text.

2.3.2 Shock Mach Number

The Mach number of CS is equally important to study shock properties and categorise them as it is with shock waves formed in ordinary gases. From the RH relations, the important velocity that is compared is the fast MHD wave velocity, while in practice the Alfvén and the magnetosonic speeds are more commonly used. It is defined as

$$M = \frac{\mathbf{V_{flow}} \cdot \mathbf{n}}{|\mathbf{V_{refVel}}|} \tag{2.5}$$

where $\mathbf{V_{flow}}$ is the velocity of the fluid relative to the shock and V_{refVel} is a reference velocity and the Mach number is named based on the reference velocity that is used. This is useful because it helps in the categorisation of various shocks as different dependencies might emerge when a different reference velocity is used. For example, if the magnetosonic $V_{ms} = \sqrt{C_A^2 + C_S^2}$ is used, then we would calculate the magnetosonic Mach number.

2.4 Resistive Shocks

As previously mentioned, in order to obtain a steady state shock, what is necessary for a steepening wave to not collapse is an energy dissipation mechanism. The dissipation mechanisms are incorporated in the MHD equations in the form of resistivity,

viscosity and thermal conductivity [Coroniti, 1970].

Each of the processes described in Coroniti [1970] is characterised by a scale length that make the magnetic and viscous Reynolds numbers equal to 1. The Reynolds numbers indicate weather a wave will be damped or if it will be able to propagate. More specifically, if the viscous Reynolds number is smaller than unity, then the viscous forces dominate and the flow is smooth, while if it is larger than unity, then waves are more free to propagate. Similarly when the magnetic Reynolds number < 1 magnetic fluctuations are smooth while for > 1 they are free to propagate. The three dissipation or diffusion scale lengths are given by

$$R_m = \frac{c^2}{4\pi\sigma V_{ph}} \tag{2.6}$$

$$R_e = \frac{\frac{4}{3}\eta + \zeta}{\rho_0 V_{Ph}} \tag{2.7}$$

$$R_t = \frac{\kappa}{\rho_0 V_{ph}} \tag{2.8}$$

where c is the speed of light, ρ_0 is the average density, η and ζ are the two coefficients of viscosity, κ is the thermal conductivity, σ is the electrical conductivity and V_{ph} is the wave phase velocity.

In all of the Eq. 2.6, 2.7 and 2.8, a larger phase velocity leads to a smaller length. When resistivity is considered, the affected terms in the dispersion relation of the linear MHD waves [see Coroniti, 1970], is the Alfvén velocity, which in turn modifies the magnetosonic speed $C_{MS}^2 = C_S^2 + \bar{C_A}^2$. The real part of the Alfvén velocity is then given by

$$Re(\bar{C_A}) = \frac{C_A^2}{1 + k^2 R_m^2} \tag{2.9}$$

where k is the wave number. As the wave phase velocity decreases, R_m becomes larger than unity and $C_{MS} \to C_S$.In order for a fast shock to be stable, according to RH jump conditions, the upstream velocity must be $V_b > V_f$ and downstream of the shock $V_f > V_b > V_i$. In the limit of $kR_m \gg 1$, $Re(\hat{C_A}) \to 0$ and so $V_f \to C_S$, while $V_s = V_i = 0$.

For the resistive dissipation, an expression can be derived that describes the evolution of the magnetic field in the tangential direction [Coroniti, 1970]

$$R_m \delta \frac{dB_z}{dx} = \frac{(\hat{V_x^2} - V_f^2)(\hat{V_x}^2 - V_s^2)}{\hat{V_x}^2(\hat{V_x}^2 - C_s^2)} \delta B_z \tag{2.10}$$

where δB_z is the perturbation about a stationary point of the magnetic field and $\hat{V_x} = V_x + \delta V$ is the perturbed bulk flow velocity in the x direction. V_x is the flow parallel to the shock normal vector and δV is the velocity perturbation.

For a fast shock, in the upstream region, $\hat{V_x}$ exceeds V_f and V_s, so Eq. 2.10 is positive, which makes the upstream point unstable. Coroniti [1970] concludes that all fast shocks can be initiated by resistivity. On the other hand, downstream of the shock, $\hat{V_x} < V_f$, which means that Eq. 2.10 will be negative. This will cause the perturbation to be damped. On the other hand, when $\hat{V_x} < C_s$ and when $\beta > 1$ ($C_S > V_s$), the magnetic field perturbations increase and therefore the downstream point is unstable and another dissipation mechanism is required to form a stable shock.

Finding when $\hat{V_x} = C_s$, defines the critical Mach number (M_{crit}). M_{crit} defines the Mach number above which a shock cannot be formed and be stable, using only resistivity as a dissipation mechanism [Kennel et al., 1985]. The critical Mach is strongly dependent on the upstream β and θ_{Bn} parameters. Edmiston and Kennel [1984] performed a parametric study and their results include a surface that shows how the first critical Mach number is modified based on these parameters. They also concluded that for typical solar wind conditions, the critical Mach number is between 1 and 2. For perpendiucular shocks in cold plasma ($\beta = 0$) the critical Mach number was found to be ~ 2.7 by Marshall [1955].

It should be noted that at subcritical shocks, other dispersion mechanisms could also be in effect along with resistivity. The M_{crit} does not identify when the dissipation mechanisms are in effect.

2.5 Subcritical Shocks

So far two methods of kinetic plasma flow energy dissipation have been discussed. Resistivity can provide enough dissipation for subcritical shocks, where subcritical shocks are characterised by a Mach number that is lower than the first critical Mach number, previously defined. On the other hand dispersion was shown from two-fluid MHD to be able to dissipate energy by removing energy from the ramp due to the difference in the wave phase velocity. These waves are phase standing in the upstream region of the shock, depending on the shock normal angle, Mach number and plasma beta. These three parameters are all included in the whistler critical Mach number, above which the whistler wave cannot phase-stand in the frame of the shock. The frame of the shock is the frame of reference that is moving with the velocity of the shock. This whistler wave train was shown to have the scales of the ion inertial length (R_i) [Coroniti, 1971]. Downstream of the shock, oscillations from the intermediate branch of the dispersion relation can also propagate, including an electrostatic sound wave. In the case the shock Mach number is above M_{wh}, then the ramp is expected to have a width of the electron inertial scale [Kennel et al., 1985; Balikhin et al., 1995].

In order to determine the scales of resistive dissipation a theory of the mechanism that is causing it needs to be examined. Resistivity is proportional to the collision frequency of the particles and inversely proportional to the electron plasma frequency. In a collisionless plasma, the collision frequency is called the anomalous collision frequency and it describes the interaction of the electrons of the plasma with non-linear waves.

One instability that could cause anomalous resistivity is the ion sound instability. The threshold for the instability to be triggered is a function of the electron to ion temperature ratio T_e/T_i. The electron drift velocity relative to the ions, generates a current whose parallel component can reduce the current flow in that direction. The growth rate of this instability in the case of $T_e \gg T_i$ is given by [e.g. see Kennel

et al., 1985]

$$\gamma = (m_e/m_i)^{1/2}(\omega/kC_S^i)^{-3}[\mathbf{k}\cdot\mathbf{V}_{De} - \omega] \tag{2.11}$$

where m_e and m_i is the electron and ion masses respectively, $\mathbf{V}_{De}$ is the electron drift velocity and $C_S^i = (T_e/m_i)^{1/2}$ is the ion sound speed. Ion sound waves will become unstable when $V_{De} > C_S^i$, which is when the electron drift velocity is larger than the ion sound waves phase velocity. The waves that are generated due to the electron motion are absorbed by the ions, which are scattered. The electron distributions becomes flattened at low velocities and the ion distribution a peak at velocities comparable to the ion sound wave velocity. For the case where $T_e \sim T_i$, then the electron drift velocity must be close to the electron thermal velocity.
Under typical solar wind conditions, where $\omega_{pe}/\omega_{ce} \gg 1$, the electron drift velocity is given by

$$V_{De}^{max} = C_S^i(\frac{m_i}{m_e})^{1/4} \tag{2.12}$$

being limited by ion sound anomalous resistance. The magnetic Raynolds length and as an extent the subcritical shock spatial scales where the excess energy is dissipated by such a mechanism, is given by [e.g. see Kennel et al., 1985]

$$\Lambda_{AIS} = \frac{c}{\omega_{pi}}(\frac{m_e}{m_i})^{1/4}\beta^{-1/2}sin(\theta_{Bn}) \tag{2.13}$$

When $\Lambda_{AIS} > R_e$, the subcritical shock will be resistive, while otherwise it will be dispersive. For a small β, cold plasma, the majority of subcritical shocks are resistive. Under typical solar wind conditions, subcritical quasi-perpendicular shocks are resistive, while quasi-parallel shocks are dispersive [Kennel et al., 1985].

2.6 Dispersive Shocks

Dispersion is one of the mechanisms that wave steepening can be limited. When considering two-fluid MHD equations, the equations that describe the dispersion of the MHD waves, describe dispersive waves. As dispersive waves propagate with different phase velocity at different wavelength/frequency, small differences in the plasma flow and state at the point where the wave steepens, can lead those waves

to radiate from steepening front. As they propagate, they will be damped by dissipation and so conversion of energy from kinetic to thermal is achieved.

In general, three important spatial scales are involved in the dispersion relation of these waves, namely the ion inertial scale length c/ω_{pi}, the electron inertial scale length c/ω_{pe} and the Debye length λ_D (defined in Chapter 1), where $\omega_{pe} = (4\pi n_e e^2/m_e)$ is the electron plasma frequency and $\omega_{pi} = (4\pi n_i e^2/m_i)$ is the ion plasma frequency. The density of each species is given by n_s and the mass by m_s, where s is either i or e for ions and electrons respectively.

In the case of perpendicular propagation, the dispersion relation from two-fluid MHD in quasi-neutral plasma is [Kennel et al., 1985]

$$\frac{\omega^2}{k^2} = C_S^2 + \hat{C_A} \tag{2.14}$$

where

$$\hat{C_A} = \frac{C_A^2}{1 + k^2 r_e^2} \tag{2.15}$$

and $r_e = c/\omega_{pe}$.

The stationary point analysis, similar to Eq. 2.10 for $\theta_{Bn} = 90°$ then gives

$$R_e^2 \delta \frac{d^2 B_z}{dx^2} + R_m \delta \frac{dB_z}{dx} = D\delta B_Z = \frac{\hat{V_x^2} - V_{MS}^2}{\hat{V_x}^2 - C_s^2} \delta B_z \tag{2.16}$$

Looking again at the transition of states for fast shocks previously described, upstream of the shock, $V_x > V_f$ and so the right-hand-side of 2.16 is positive. The solution of 2.16 that does not violate the condition that δB_z tends to 0 far upstream of the shock is then the positive root of *lambda*

$$\delta B_z \sim e^{\lambda x} \tag{2.17}$$

$$\lambda = \frac{-R_m + (R_m^2 + 4R_e^2 D)^{1/2}}{2R_e} \tag{2.18}$$

The conclusion is that the spatial scale of the shock ($\Lambda = 1/\lambda$) is given by

$$\Lambda \sim \begin{cases} \frac{R_e}{D(V_u)} & , R_e \gg R_m \\ \frac{R_m}{D(V_u)} & , R_m \gg R_e \end{cases} \tag{2.19}$$

where V_u is the upstream bulk flow velocity in the shock normal direction. Which translates to the thickness of the shock being dependent on the larger dissipation scale, in this case the magnetic Reynolds number or the electron inertial length.

For the case where $R_e \gg R_m$, the bulk flow velocity is $V_b > V_S$, but $V_b < C_{MS}$, downstream of subcritical shock, since $C_M \sim C_S$ for critical shocks. This means that $D(V_d) < 0$, where V_d is downstream shock velocity in the normal direction. In the case of a supercritical shock, downstream of the shock $D(V_d) > 0$.

So for subcritical perpendicular shocks ($\theta_{Bn} = 90°$), downstream of the shock we expect to find a trailing wave that is weakly damped by resistivity. Downstream of supercritical shocks we expect steepening to continue until a different dissipation mechanism completes the transition, since λ grows with distance from the shock front.

When the shock steepens at the Debye length the quasi-neutral approximation is not valid. At scales smaller than the electron inertia scale, current oscillations are decoupled from the magnetic field oscillations. This will lead to a nonlinear ion sound wave train to be formed downstream of the supercritical shock [Kennel et al., 1985; Balikhin et al., 1995]. This wave cannot be damped by resistivity alone.

For oblique propagation, it is useful to examine the dispersion relations of the two-fluid MHD waves for low and high β separately as seen in Formisano and Kennel [1969].

Table 2.1 shows the dispersion relation that describes each wave for different frequency ranges and are derived by the dispersion plots in Formisano and Kennel [1969]. The dispersion relation for each wave is obtained by solving the general two-fluid dispersion relation under different assumptions.

At the ion cyclotron and electron cyclotron frequencies, different modes interact with each other. The interaction between the two waves is where their phase velocities are equal. At the first interaction point as the frequency and wavenumber increases (Ω_{ci}), the intermediate wave interacts with the slow wave. This leads to the intermediate wave slowing down and becoming the electroacoustic wave. The slow wave resonates at the ion cyclotron frequency and it does not propagate, as it

Table 2.1: Waves dispersion relations in terms of frequency ranges for $\frac{C_S}{C_A} \ll 1$

	Fast Magnetosonic	$\frac{\omega}{k} \sim \sqrt{C_A^2 + C_S^2 sin(\theta_{kB})^2}$	$\Delta V_{ph} > 0$
	Intermediate Wave	$\frac{\omega}{k} \sim C_A cos(\theta_{kB})$	$\Delta V_{ph} < 0$
	Slow Wave	$\frac{\omega}{k} \sim C_S cos(\theta_{kB})$	$\Delta V_{ph} < 0$
Ω_{ci}			
	Whistler	$\frac{\omega^2}{k^2} \sim C_A^2 \frac{\omega cos(\theta_{kB})}{\Omega_{ci}}$	$\Delta V_{ph} > 0$
	Electroacoustic	$\frac{\omega}{k} \sim C_S$	$\Delta V_{ph} = 0$
Ω_{ce}			
	Acoustic Mode	$\frac{\omega}{k} \sim C_S$	$\Delta V_{ph} = 0$

is damped. A wave resonates when for k the frequency remains finite, which leads to a zero phase velocity as the wavenumber grows. At the second interaction point in the dispersion relation, the electron cyclotron frequency, the whistler wave interacts with the electrostatic wave. At this point the whistler is slowed down to C_S and the electrostatic wave stops propagating, as it resonates.

Formisano and Kennel [1969] define a positive dispersion when the phase velocity increase with an increasing wavenumber, and the opposite defines a negative dispersion. The branches of the dispersion relation have a different dispersion sign as shown in Table 2.1. The Fast magnetosonic and whistler branches of the dispersion relation have a positive dispersion, while the rest of the branches have a negative one. As the β parameter increases, the point of interactions, the resonant frequencies, are modified. Specifically the interaction point of the intermediate with the slow wave is increase to frequencies higher than Ω_{ci}. The intermediate wave has a positive dispersion for scales $\sim c/\omega_{pi}$. The branch of the dispersion relation that is related to the fast magnetosonic wave is for the bigger part the same, since they are electromagnetic circularly polarized waves, whose dispersion is governed by the finite ion inertia [Formisano and Kennel, 1969]. The interaction point for higher β plasma, is given as $\frac{\omega cos(\theta_{kB})}{\Omega_{ci}} \sim \frac{C_S^2}{C_A^2}$, after equating the cold plasma whistler dispersion with the sound speed [Formisano and Kennel, 1969]. As the plasma β increases, the frequency and wavenumber of the interaction point will also increase. As the β increases even further, the ion inertia decouples from the oscillations of the magnetic

field, as thermal pressure becomes more important than the magnetic one. This leads the sound velocity to be larger than the whistler wave phase velocity and the two branches do not interact.

Since the fast branch phase velocity increases with decreasing wavelength, upstream of oblique shocks, a wave train will exist. In the upstream region of a shock, the ion inertial scale length, as defined by Coroniti [1971], is given by

$$R_i = \frac{c}{\omega_{pi}} \frac{C_A cos(\theta)}{V_u} \tag{2.20}$$

Comparing the upstream ion inertial length to the electron one, previously defined (R_e), when $R_i > R_e$ a wave train will lead the shock and when $R_i < R_e$ the wave train will be downstream of the shock. The condition $R_i = R_e$, defines the angle where the structure of the shock changes

$$cos(\theta_c) = \sqrt{\frac{m_e}{m_i}} M_A \tag{2.21}$$

where M_A is the Alfvén Mach number, and m_e and m_i are the electron and ion masses respectively. For low β and low Mach number, $\theta_c \sim 87°$, which means in the majority of oblique shocks will have a wave train upstream of the shock.

2.7 Supercritical Shocks

The structure of supercritical shocks, as is the case for subcritical shocks, depends greatly on the shock normal angle. Interplanetary shocks are formed by counter-streaming plasmas of when streams propagate at relative velocity larger than the magnetosonic speed. Contrary to interplanetary shocks, planetary bow shocks form due to the supersonic solar wind encountering a planetary magnetosphere as it propagates outwards from the Sun. For example, the Earth's magnetic field is parabolically shaped and at 1AU distance from the Sun, the interplanetary magnetic field, that originates from the Sum, cuts the Earth-Sun line at $\sim 45°$. A simplified illustration can be seen in Figure 2.2, where the vast range of angles, between the shock normal and the upstream magnetic field, at the bow shock can be found. The Earth's rotation around the Sun also changes the global θ_{Bn} that can be observed

by a satellite at a given orbit. This means different types of shocks can be observed throughout the year from the same spacecraft.

A high level distinction at this point can be made between the quasi-parallel and

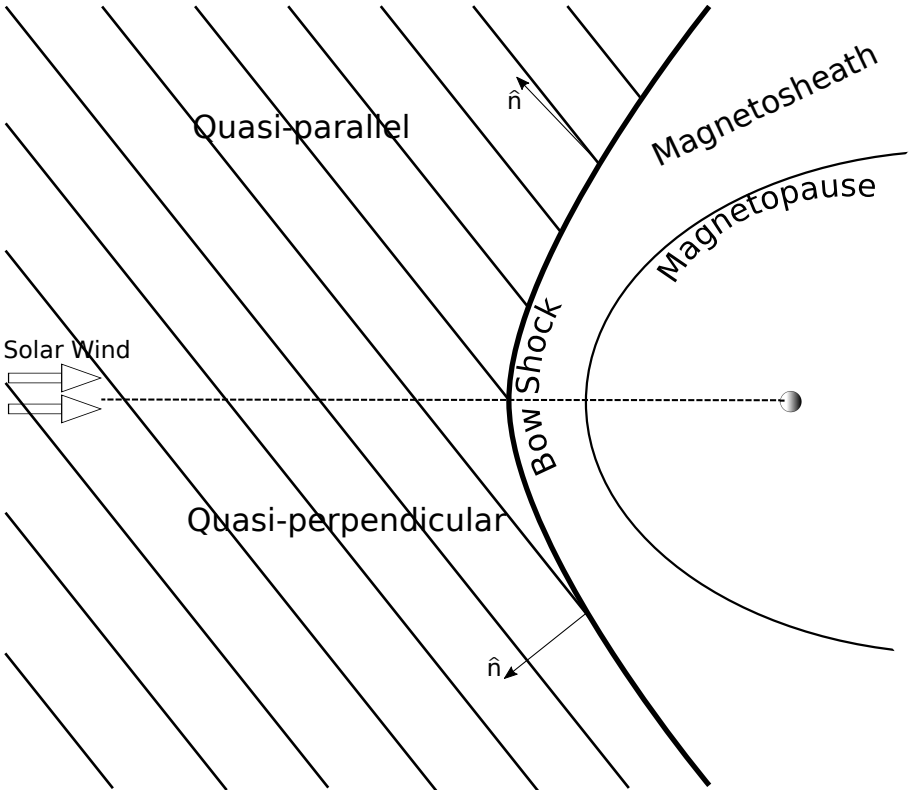

Figure 2.2: Simplified illustration of the Earth magnetic field environment. The elements of the figure are not to scale with the actual distances.

quasi-perpendicular shocks, which will be described separately. Macroscopically, the main differences between the quasi-parallel and quasi-perpendicular shocks is that the former are more turbulent and it is difficult to determine the transition layer between upstream and downstream. While for quasi-perpendicular shocks, the shock ramp is more abrupt and easier to distinguish. On the side where the Earth's quasi-parallel bow shock region is located, a *foreshock* region has also been observed. The foreshock region is a region where reflected particles from the parallel shock stream freely upstream and electromagnetic waves of different amplitudes and frequencies can be observed. Because of these waves, distinguishing between the upstream and downstream region is difficult. The difference of the shape of supercritical shocks with the one predicted by the theory for subcritical shocks and the new regions that

appear to be common among similar types of supercritical shocks, are a result of the processes that are required to complete a supercritical shock transition.
The following sections will provide some background on the quasi-perpendicular and quasi-parallel shocks and the foreshock.

2.7.1 Foreshock

The foreshock is the region of space in front of the shock where reflected particles stream upstream into the incoming flow. In the case of quasi-perpendicular shocks, the foreshock consists of gyrating ions, that form a region upstream of the shock also known as the foot. In the case of quasi-perpendicular shocks, this region extends much further upstream. In the geometry of the Earth's bow shock, the upstream region where - macroscopically considering the interplanetary magnetic field and the hyperbolic shape of the shock - the bow shock is quasi-parallel, is separated into the electron and the ion foreshocks. In the electron foreshock backstreaming electrons are observed, while in the ion foreshock, the main population of particles that originate from the bow shock are of the ion species. The electron foreshock is situated further upstream of the ion foreshock, due to the larger electron velocity parallel to the magnetic field compared to the ions. Along with these particles, large magnetic field fluctuations are observed in these regions.
The ion populations in the foreshock have been separated into three categories based on their distribution into *reflected* (more commonly called field-aligned), *intermediate* and *defuse* by Paschmann et al. [1981]. Field-aligned ions have the distribution of a fast ion beam with a temperature of $[1-4]10^6\,K$ and $5V_{Sw}$ speed. Diffuse ions have a distribution that appears as a ridge and occupy larger area of the phase space with temperature $> 10^7\,K$. Intermediate ions are described by a crescent shaped distribution. Paschmann et al. [1981] hypothesised that the intermediate ions originated from pitch angle scattered reflected ions and in turn wave particle interactions formed the diffuse ions, although that was later shown not to be the case [see Burgess et al., 2005].
In the electron foreshock, field-aligned beams are also found near the leading edge

of the foreshock and the angular distribution of the more energetic electrons become diffuse closer to the bow shock [see Kennel et al., 1985].

The foreshock is a very turbulent region where different waves can be found, some of which are hypothesised to be linked to the ions. One type is large amplitude ($\Delta B/B \sim 1$) low frequency waves ($\sim 0.03\,Hz$) that are hydromagnetic, are magnetically connected with the bow shock and have been linked to back-streaming ions [Fairfield, 1969; Hoppe et al., 1981]. A second type of waves, identified by Russell et al. [1971], are wavepackets with a frequency $\sim 0.4\,Hz$ that were reported to have a fast growth rate and a slow decay rate. They were observed to propagate upstream of the bow shock with an angle between the solar wind velocity and background magnetic field and are convected downstream by the solar wind. After reversing the doppler shift that the waves underwent in the spacecraft frame, it was found that they are right-hand polarised with a frequency $\sim 10\omega_{pi}$. A third type of wave in the frequency range $0.5 - 5\,Hz$ and with amplitude $\Delta B/B \sim 0.2$, has been characterised as circularly polarized whistlers and are observed adjacent to the bow shock [Fairfield, 1974]. These waves were also reported to propagate obliquely relative to the background magnetic field with $\theta_{kB} \sim 20° - 40°$. A fourth type of waves found in the foreshock are relatively higher frequency ($1\,Hz$) small amplitude ($\Delta B/B \sim 0.1$) waves [Hoppe et al., 1982]. After being Doppler shifted they were found to be right-handed whistler mode waves with a plasma rest frame frequency $\sim 20 - 100\,\omega_{ci}$. They were observed to propagate at highly oblique angles $\sim 45°$.

The presence of these particle populations and waves in the foreshock ahead of the quasi-parallel shock are thought to be connected with the dissipation processes in these types of shocks as well as particle acceleration by the shock. This region is of great interest as cosmic rays have been hypothesised to consist of particles accelerated from astrophysical shocks [Blandford and Eichler, 1987].

2.7.2 Quasi-perpendicular Shocks

Provided the clear transition from upstream to downstream region, quasi-perpendicular shocks are far better understood than quasi-parallel, since there have been more

studies examining their properties. Quasi-perpendicular shocks consist of the *foot*, *ramp*, *overshoot* and *undershoot* regions. The ramp is the steepest part of the front, while the foot is a less steep region where the magnetic field increases linearly.

The structure of supercritical quasi-perpendicular shocks is largely related to ion reflection of a fraction of the incoming ions [Kennel et al., 1985]. When reflected, these ions move upstream of the shock until they are overturned again, by the magnetic field and are directed again towards the shock. This process is observed in the form of a magnetic foot [Woods, 1971]. The ions that are overturned gain energy due to the transverse electric field and are able to cross the shock. Downstream of the shock, the ions gyrate in the overshoot region and they are convected further downstream. This mechanism provides dissipation of the energy of the incoming flow and heats the ions.

As previously stated, the spatial scales of the shock determine the physical processes based on the scales that they are comparable with. The spatial scales of the magnetic ramp of quasi-perpendicular shocks were believed to be of the order of the ion inertial scale length c/ω_{ci}, but it has been shown that the more accurate measure is the convective ion gyroradius given by V_{Sh}/ω_{ci}^{d} (d denotes downstream value). This can be seen when larger Mach number shocks are considered $M_{ms} \geq 4$, where the two quantities begin to differ substantially, while they are of similar magnitude for $M_{ms} < 4$. When expressed in terms of the ion inertial length, across the same range of M_{ms}, the spatial scale of the shock has a much wider range. For $M_{ms} \geq 4$, the authors find that the scale of the shock is $\sim 0.4 V_{Sh}/\omega_{ci}^{d}$.

The overshoot region is followed by an undershoot region which appears as a wave-train in magnetic field measurements. Livesey et al. [1982] noted the appearance of the overshoot feature of the shock when the Mach number surpasses the critical Mach number and that an increase in the amplitude of the overshoot is followed by increase of M_f/M_c and β. This region has been shown to be linked with reflected and heated ions, which govern the structure of the shock [Leroy et al., 1982]. Initially the size of the overshoot-undershoot region was considered to scale with the ion Larmor radius [Kennel et al., 1985], but it was later shown that, similar to

the ramp, the convected ion gyroradius of the trapped population in the overshoot region better describes scale [Bale et al., 2005]. Saxena et al. [2005] conducted a study on the overshot-undershoot spatial scales, by examining the decay rate of the overshoot region by fitting an exponent to the density at the region of the overshoot. Inside the overshoot regions, ions are trapped and the structure of the region is associated with this motion. The results show that the wavelength of this region does not scale to the ion inertial length, but instead the convected ion gyroradius given by V_{sh}/ω_{ci}, where ω_{ci} is calculated for downstream values and V_{Sh} is the velocity of the shock in the normal direction.

The foot region, which appears as a region of linear increase with a much less steep than the main magnetic ramp, is also a region found in supercritical quasi-perpendicular shocks. This region has also been linked to ion reflection and at the edge of this magnetic foot, the reflected ions are overturned. Gedalin [1996] also argues that the ion reflection process, apart from the upstream and downstream plasma parameters, also depends on the structure of the individual shock. This is because the dissipation will be affected based on the amount of particles that are specularly reflected and the ones that are non-specularly reflected.

A second critical Mach number exists (M_{c2}), which defines when reflecting shocks begin to occur. Woods [1971] also offers an estimate on M_A, where reflecting shocks begin to occur, based on experimental data. The second critical Mach number can be calculated analytically by assuming a downstream velocity equal to the ion sound velocity downstream of the shock in the RH equations [Leroy et al., 1982]. M_{c2} heavily depends on the dowstream electron to ion temperature ratio and the upstream plasma β, as well as on the θ_{Bn} angle. This dependence is illustrated in Kennel et al. [1985], where M_{c2} has been calculated for three different downstream values of T_e/T_i with respect to β_i and θ_{Bn}. The critical Mach number ratio M_{c2}/M_c has also been calculated with $\beta_i = 1$ and for a range of T_e/T_i. As the temperature anisotropy between electrons and ions increases, the critical Mach number ratio also increases. It is also argued that at a third critical Mach number, ion reflection will not be able to dissipate the excess energy and the shock will no longer be stable [Kennel et al.,

1985].

[Morse et al., 1972] conducted laboratory experiments on supercritical shocks with M_{ms} ranging between $4-8$ and observed that the shock was oscillating with a frequency comparable to ω_{ci}. Lobzin et al. [2007] conducted a study of high Mach number shocks ($M_A \sim 2-12$) and determined that this frequency ranges between $[0.3-1]\omega_{ci}$ and the occurrence of non-stationary shocks increased as M_A increased. A proposed theory on the processes that cause non-stationarity are described in Krasnoselskikh et al. [2002], where in supercritical shocks, the magnetic ramp is treated as a nonlinear whistler wave. The model of this theory is presented in Krasnoselskikh [1985], where the nonlinear motion of hydrodynamic waves that break at high mach numbers is examined. When the shock front is modelled as a nonlinear whistler wave, at high Mach numbers, specifically above the nonlinear whistler Mach number, the nonlinear wave train cannot exist within the shock front. This is the result of inadequate dissipation due to resistivity or dispersion to accommodate the high incoming flow energy and the wave train is overturned. At the regions where the wave is now broken, the density of the reflected ions is higher, the plasma is turbulent and the energy can be dissipated faster [Krasnoselskikh, 1985].

Finally it is useful to note that the shock non-stationarity is also expressed in terms of magnetic field profile spatial and temporal variations and in the particle distribution. These variations have been observed by the Cluster spacecraft, where even though they are closely separated in some examples, the differences still exist [e.g. see Bale et al., 2005].

2.7.3 Quasi-parallel Shocks

Quasi-parallel shocks ($\theta_{Bn} < 45°$) have not been very well studied due to the difficulty in differentiating the various regions that characterise a shock. It is difficult to determine the location of the transition from the upstream to the downstream medium from magnetic field measurements due to the turbulent nature of these type of shocks. From single spacecraft missions, this is an even harder task, while multi-spacecraft missions might be able to provide a better insight into the structure of

the magnetic field.

Because of the magnetic field geometry, particles that encounter quasi-parallel shocks in the downstream region, can on average free stream through it preserving their magnetic moment when they move parallel to the magnetic field. For θ_{Bn} a significant amount of ions are allowed to escape the downstream region into the upstream region [Edmiston et al., 1982]. A critical Mach number at which significant numbers of ions can free stream towards the upstream region of the shock is given by $V_d = 3C_i^d cos(\theta_{Bn}^d)$, where in this case θ_{Bn}^d is the angle between the shock normal vector and the downstream average magnetic field [Kennel et al., 1985]. These particles that escape can interact with the foreshock waves.

In quasi-parallel shock geometries, measurements have shown temporal variations in the geometry of the shock. This can be seen from multiple spacecraft missions that are closely separated when the normal vector calculated using Minimum Variance Analysis (MVA) for each of the spacecraft yields very different result. Provided that the MVA is sufficiently well defined, in terms of eigenvalues and it satisfies the $\mathbf{B} \cdot \mathbf{n} = const$ condition, this is indicative that the spacecraft have encountered a three dimensional structure. These structures are often referred to as SLAMS (Short Large Amplitude Structures) and have been encountered at quasi-parallel shocks [Schwartz and Burgess, 1991].

SLAMS have been associated with the ultra low frequency (ULF) waves, previously described in the foreshock region of the shock, but it has been shown that their scales are smaller than those of the ULF waves [see Burgess et al., 2005]. These structures often appear to have spatial scales of the radius of the Earth and could explain the unclear shock crossing that is observed in quasi-parallel shocks. These structures also appear to have substructures on the scales of $\sim 600\,Km$ [Behlke et al., 2003]. In the study it was also found from the combination of electric and magnetic field data that SLAMS move with the same velocity as the plasma and so ions are trapped inside. These structures are important since they are expected to interact with the solar wind and they might play a role in particle reflection and acceleration.

2.8 The Earth's Magnetosheath

The Earth's magnetosheath, which is the region of interest of Chapter 4, is the region in space between the Earth's bow shock and the Earth's magnetopause, the boundary between the solar wind and the Earth's magnetosphere. It consists of particles that have been decelerated by the bow shock and a smaller portion of particles from the magnetosphere. The plasma characteristics in the region are strongly dependant on position in terms of distance from the bow shock and the magnetopause. The downstream region of quasi-perpendicular shocks is different from the one in quasi-parallel shocks since the particles are heated in a different manner. In addition, the shape of the Earth's magnetosphere also plays a role in how the plasma is deflected around it, so plasma parameters are also different along the Sun-Earth axis and in the flanks of the magnetosheath.

The average properties of the plasma in the magnetosheath have been documented by spacecraft measurements and some characteristics summarised by Lucek et al. [2005], based on the results of Kivelson and Russell [1995]; Phan et al. [1996, 1997]; Hill et al. [1995]; Li et al. [1995]. Some average properties can be summarised as

- The average density and magnetic field are higher than in the solar wind following the RH relations upstream and donwstream of the shock
- The average flow is directed in an oblique angle from the Sun-Earth axis and is diverted around the magnetopause
- Donwstream of the shock, the bulk flow velocity is smaller than V_f
- The flow increases to supersonic velocity near the flanks
- The ion temperature is increased compared to the solar wind
- The electron temperature is higher than that of the solar wind electrons
- The ion temperature is higher than the electron $\sim 6 - 7$ times on average
- β has large variations across the region

- A perpendicular to parallel temperature anisotropy is present and increases as the plasma flows from the bow shock to the magnetopause.
- The ion temperature anisotropy is more pronounced than the electron temperature anisotropy

It is clear that in different regions of the magnetosheath, different turbulence is expected to be observed.

An initial separation of the observed fluctuations can be made between lower and higher frequency. In the low frequency regime, downstream of the bow shock, the intrinsic solar wind turbulence is one of the sources of turbulence, which has been modified by the shock [Lucek et al., 2005]. Fluctuations that originate from the particles in the foreshock region, with a velocity lower that the solar wind bulk flow are also convected downstream by the solar wind [Paschmann et al., 1981]. In the case of quasi-perpendicular shocks, ion populations that gyrate downstream of the shock can produce low frequency waves [Horbury et al., 2001; Sckopke et al., 1983]. Due to the varying temperature anisotropy and β, different instabilities can be initiated, which in turn generate waves. The ion cyclotron instability and the mirror mode instability can be found behind the weaker quasi-perpendicular bow shocks and strong quasi-perpendicular shocks respectively [Schwartz et al., 1996; Kivelson and Southwood, 1996]. The ion cyclotron instability requires high ion temperature anisotropy and $\beta \sim 1$ while the mirror instability is more likely to occur under moderate temperature anisotropy and high β. The ion cyclotron instability excites electromagnetic transverse waves with a velocity $\sim C_A$ that propagate away from the source. On the other hand, mirror modes are spatially extended structures that do not propagate relative to the bulk plasma flow and are characterised by anti-correlated magnetic field magnitude and density changes. are anti-correlated with fluctuations of the magnetic field and the density.

Some higher frequency waves observed in the magnetosheath are electromagnetic emissions known as lion roars, which are examined in Chapter 4, and electrostatic waves, referred to as broadband electrostatic noise [Rodriguez, 1979].

The electrostatic emissions frequencies are found throughout the magnetosheath and their frequency ranges between $20\,Hz$ to $70\,kHz$. The emissions consist of three components at different frequencies, a high frequency component that exceeds $30\,kHz$ and peaks at the electron plasma frequency, a not well defined intermediate component with frequency between f_{pi} (ion plasma frequency) and f_{pe} (electron plasma frequency), the ion and electron plasma frequency respectively, and a third, low frequency component, with a peak lower than the f_{pi}. According to Rodriguez [1979] the low frequency component is associated with the bow shock, due to their polarisation parallel to the magnetic field, where the ion heating initially occurred and continued throughout the magnetosheath. The high and intermediate frequency components are not correlated with the shock and are less likely to be observed at dawn and dusk.

Chapter 3

Collisionless Shock Velocity

3.1 Introduction

As described in the previous chapter, the spatial scales of collisionless shocks is important in the determination of the dissipation mechanisms that are responsible for preventing the wave breaking and maintaining a steady shock [Kennel et al., 1985; Balikhin et al., 1995]. The scale of the shock governs the interaction of the charged particles and the fields within the shock itself. Adiabatic thermalisation of electrons is expected in the case of a large shock front, while in the case of smaller ramp widths the electrons are heated non-adiabatically. This type of energization was found to exceed the adiabatic one in some cases [Balikhin and Gedalin, 1994; Gedalin et al., 1995]. Gedalin et al. [1995] also describes how this energization is translated to energy transfer from the cross-shock potential to electron gyration downstream of the shock.

In order to determine the scales of a shock several methods can be employed. The availability of the methods that can be used largely depends on the number of closely separated spacecraft, available to make measurements of the same shock. Unfortunately multi-spacecraft missions are available in very limited cases so far. From single spacecraft measurements, a simple in conception but hard in practice method, that can be employed is by measuring the velocity of the shock (V_{Sh}). This velocity can then be used to determine the length of the shock ramp in the normal direction, based on the time required for the spacecraft required to cross the shock

front.

With the use of multi-point measurements provided by multi-spacecraft missions such as ISEE, AMPTE, Cluster and THEMIS, spatial and temporal ambiguity can be resolved. This allows the determination of the speed of the shock relative to the spacecraft and hence, the spatial scales of the shock front. Currently, only the terrestrial bow shock has been subjected to multi-point measurements, while planetary missions lack this ability. It is however important to study planetary bow shocks as they significantly expand the variety of shock parameters that are complementary to terrestrial bow shock data. For example, the detection of a purely kinematic shock at Venus was reported [Balikhin et al., 2008], which has not been previously reported.

In this chapter it is of interest to determine the accuracy of two proposed methods, one by Moses et al. [1985] and one by Gosling and Thomsen [1985], that make use of the shock foot region to determine V_{Sh}, from single spacecraft measurements. The foot region was first identified by Woods [1969], where it was shown that in front of super-critical, quasi-perpendicular shocks, the foot region is observed as a result of the reflected ions from the shock itself. When the angle between the normal vector to the shock surface ($\mathbf{n}$) and the upstream magnetic field ($\mathbf{B_u}$) is greater than 45°, the shock is characterised as quasi-perpendicular. In super-critical CS, the Mach number of the shock exceeds the first critical Mach number, above which anomalous resistivity cannot provide the required energy dissipation Kennel et al. [1985].

Both methods use analytical expression for the width of the foot which combined with magnetic field observations of the foot can yield an estimate of the relative to the spacecraft velocity of the foot. V_{Sh} is then assumed to be the same, given that the foot structure will have the same velocity as the shock, relative to the spacecraft. The accuracy of the estimates of the two methods mainly depends on the accuracy of the analytical expression for the foot width. Moses et al. [1985] makes use of the analytical expression for the foot width derived by Livesey et al. [1984], where the result of the predicted foot width by Woods [1971] was generalised to shock geometries other than perpendicular ($\theta_{Bn} = 90°$). On the other hand Gosling and

Thomsen [1985] define the trajectory of the reflected ions in the deHoffman-Teller frame (HT), where the solar wind velocity is parallel to the upstream magnetic field. The trajectories are then decomposed in parallel and perpendicular directions of the magnetic field and the foot width is defined by the distance as a function of time, at the time that the ions turnaround. The analytical comparison of the two methods by Gosling and Thomsen [1985] shows that the difference, of the foot width estimates, of the two methods will increase as θ_{Bn} decreases.
The estimated V_{Sh} of the two methods is then compared with the measured velocity from two spacecraft Cluster measurements. In order to ensure that the velocity from two spacecraft is measured correctly, the main consideration to be taken is that the shock is not accelerating and that its geometry is not changing between the two observations. Therefore the normal vector of the shock estimated by each of the two spacecraft must be close and the separation between the two spacecraft must not be too large. Finally the two spacecraft must not cross the shock simultaneously.

3.2 Instrumentation

Measurements of the terrestrial bow shock were obtained from the Cluster spacecraft, launched in 2000. The data used in this chapter are obtained from measurements of the Cluster between the years 2012-2014. The four satellites initially had a highly elliptical orbit of about $4\,R_E$ perigee and $19\,R_E$ apogee, with an inclination of $90\,^\circ$. The orbits of the four spacecraft have been modified several times, in order change the separation between the spacecraft. Throughout the course of the mission, the orbit has evolved enabling greater coverage. The Cluster spacecraft orbit in a variable tetrahedron formation which ranges from about $10000\,km$ to $6\,km$ distance between spacecraft. Magnetic field measurements were obtained from the Cluster Fluxgate Magnetometer (FGM) [Balogh et al., 1997], which offers data sampled at $22\,Hz$ and $67\,Hz$ in normal and burst mode respectively. Measurements of the shock ion distributions were obtained by the time-of-flight Composition and Distribution Function analyser (CODIF) of the Cluster Ion Spectrometry (CIS) ex-

periment [Rème et al., 1997]. Finally the Waves of High frequency and Sounder for Probing of Electron density by Relaxation (WHISPER) experiment [Décréau et al., 1997] was used to obtain the local electron plasma frequency in order to estimate the upstream plasma density. The review of Cluster data based advances in the physics of quasi-perpendicular collisionless shocks is given in Krasnoselskikh et al. [2013].

The Venusian bow shock measurements were obtained by the VEX spacecraft. It was launched in November 2005 and arrived at Venus in April 2006, where it was set in a polar orbit. The orbit of VEX is elliptical with apoapsis of 63000 km, a periapsis of 460 km and a period of 24 $hours$. The magnetic field measurements were obtained by the VEX fluxgate magnetometer (MAG) [Zhang et al., 2005, 2006]. MAG obtains measurements at a frequency of up to 32 Hz. Due to the noise induced by the VEX spacecraft hardware in the magnetic field measurements, the data were cleaned using the method proposed by Pope et al. [2011], which results in a data rate of 1 $vector/sec$. The upstream solar wind (SW) conditions were obtained by the Analyser of Space Plasmas and Energetic Atoms (ASPERA-4) instrument [Barabash et al., 2007].

3.3 Methodology

The foot of the shock is the region located upstream of the shock main ramp and is formed by gyrating ions reflected by the shock [Woods, 1969]. The foot appears in front of shocks that are of relatively low Mach number, super-critical and quasi-perpendicular. The two methods that are examined here, one by Moses et al. [1985] (Method $\boldsymbol{A}$) and one by Gosling and Thomsen [1985] (Method $\boldsymbol{B}$), make a prediction on the velocity of the shock, based on the width of the foot in front of the shock front.

Moses et al. [1985] noted that if the length of the foot (d_{ft}) is known, then the traversal time of the foot (Δt_{ft}) is given by Eq. 3.1.

$$\Delta t_{ft} = \frac{d_{ft}}{V_{Sh} \pm V_u cos(\theta_{Vn})} \tag{3.1}$$

where V_u is the solar wind speed, V_{Sh} is the shock speed in the normal direction and θ_{Vn} is the angle between the solar wind and normal to the shock vector. Moses et al. [1985] then used the expression that Livesey et al. [1984] developed to predict the width of the foot (d_{ft}^L), assuming only specular reflection occurs (Eq. 3.2).

$$d_{ft}^L = 0.68 \frac{\mathbf{V}_u sin^2(\theta_{Bn})}{\omega_{ci}} \cdot \hat{\mathbf{n}} \tag{3.2}$$

After the correction noted by Gosling and Thomsen [1985], the expression proposed by Moses et al. [1985] is given in Eq. 3.3.

$$V_{Sh}^A = V_u cos(\theta_{Vn}) \frac{x_L}{1 \pm x_L} \tag{3.3}$$

where

$$x_L = 0.68 \frac{sin^2(\theta_{Bn})}{\omega_{ci} \Delta t_{ft}} \tag{3.4}$$

θ_{Bn} is the angle between the upstream magnetic field and the normal vector, ω_{ci} is the ion cyclotron frequency and $\hat{\mathbf{n}}$ is the shock normal.

Gosling and Thomsen [1985] used the deHoffman-Teller frame, in which the $\mathbf{V}_u \times \mathbf{B}$ electric field vanishes, to obtain the expression in Eq. 3.5 for the foot width (d_{ft}^G).

$$d_{ft}^G = \frac{\mathbf{V}_u \cdot \hat{\mathbf{n}}}{\omega_{ci}} f(\theta_{Bn}) \tag{3.5}$$

where

$$f(\theta_{Bn}) = \omega_{ci} t_{ot} (2cos^2(\theta_{Bn}) - 1) + 2sin^2(\theta_{Bn}) sin(\omega_{ci} t_{ot}) \tag{3.6}$$

$$cos(\omega_{ci} t_{ot}) = \frac{1 - 2cos^2(\theta_{Bn})}{2sin^2(\theta_{Bn})} \tag{3.7}$$

and t_{ot} is the time it takes for the ions to be overturned by the incoming solar wind after they are reflected and all other quantities are the same as previously used. Applying the expression for the foot width in Eq. 3.5 in 3.1, the shock velocity is then given by Eq. 3.8 and 3.9.

$$V_{Sh}^B = V_u cos(\theta_{Vn}) \frac{X_G}{1 \pm X_G} \tag{3.8}$$

where

$$X_G = \frac{f(\theta_{Bn})}{\omega_{ci} \Delta t_{ft}} \tag{3.9}$$

The positive sign is used for a downstream to upstream (outbound) transition of the shock and the negative for an inbound transition.

There are limitations on the observations these methods can be applied to. The foot must exist ahead of the shock and must be clearly identifiable. This means that we are limited to quasi-perpendicular shocks. In order to be able to accurately calculate the velocity of the shock using multiple spacecraft, the spacecraft need to be relatively closely separated so that the velocity of the shock can be considered as constant. On the other hand, the spacecraft must not be too close to each other, in order to avoid large errors resulting from small changes in the estimation of the main ramp location. Another important factor is the angle between the spacecraft separation vector and the shock normal which must not be close to perpendicular, which would lead to large errors.

In order to compare the results of the two methods, the relative error (RE), defined in Eq. 3.10, will be considered.

$$RE = |\frac{|V_{Sh}^{est}| - |V_{Sh}^{obs}|}{|V_{Sh}^{obs}|}| * 100\% \tag{3.10}$$

where V_{Sh}^{est} is the estimated velocity of the shock using the expressions of either **A** (Eq. 3.3) or **B** (Eq. 3.8), V_{Sh}^{obs} is the shock velocity measured by the two spacecraft along the average normal vector ($\mathbf{n_{avg}}$) of the two spacecraft. Given two vectors $\mathbf{a} = [a_x, a_y, a_z]$ and $\mathbf{b} = [b_x, b_y, b_z]$, the average vector is $\mathbf{ab} = [(a_x + b_x)/2, (a_y + b_y)/2, (a_z + b_z)/2]$ and the angle between them is given by $\theta_{ab} = cos^{-1}(\mathbf{a} \cdot \mathbf{b})$.

The normal of the shock is calculated using minimum variance analysis of the magnetic field (MVA). The eigenvectors of the magnetic variance matrix $M_{nm} = < B_n B_m > - < B_n >< B_m >$, where $n, m = 1, 2, 3$, are orthogonal and correspond to the maximum, intermediate and minimum variance directions of the magnetic field. The eigenvector that corresponds to the minimum variance direction is also **n**. The ambiguity of the direction of the eigenvectors in our case is solved by defining that the normals of the shock point towards the upstream region of the shock.

3.4 Cluster Spacecraft Observed Shock Examples

Two examples of observations of pairs of shock crossings, that where included in the study, are presented in this section. In the first instance, the foot in front of the shock is identified. The shock normal vector was then estimated using MVA on all four Cluster spacecraft magnetic field measurements for the event in question. In the cases where the magnetic field profile appeared similar and the angle between the normal vectors for each pair was found to be less than 75°, the event was kept. If no pair combination could be found with these conditions, the sample was discarded.
In figures 3.1 and 3.2, the magnetic field intensity (blue solid line), the projection of the magnetic field along the normal vector (yellow solid line) and the two sided unweighted simple moving average of N measured points (N pt. SMA), red solid line, are plotted for each spacecraft for each of the pairs for the two examples. The main shock ramp is shown for each shock of figures 3.1 and 3.2 between the green vertical dashed lines and the foot, where observed, is between the vertical dashed red lines.
The N pt. SMA was included to assist in the identification of the linear increase in front of the ramp that defines the foot. The two sided n -point unweighted SMA $\hat{x}_p$ for a particular sample p is defined as $\hat{x}_p = \frac{1}{n}\sum_{i=-\frac{n-1}{2}}^{\frac{n-1}{2}} x_{p+i}$, where x_p is the measured value at sample p and n is odd. For the initial and final values where a sample does not exist, the measured value is assumed as 0. The number of points that are chosen depends on the magnetic field profile of the individual shock, with the consideration not to use too many points, because measurements from the downstream region will be combined with the foot. For example, if the measurements obtained from the Cluster instruments are sampled at $22Hz$, this corresponds to 22 vectors per second. If the ramp of the shock is $3\,sec$ and the filter is chosen to have $N = 45$, then the last point of the foot will consist of 22 points from the main magnetic ramp, which is one third of the ramp points. This could make the foot appear longer than it actually is.

3.4.1 Example 1 : 9 March 2012 11:25 UT

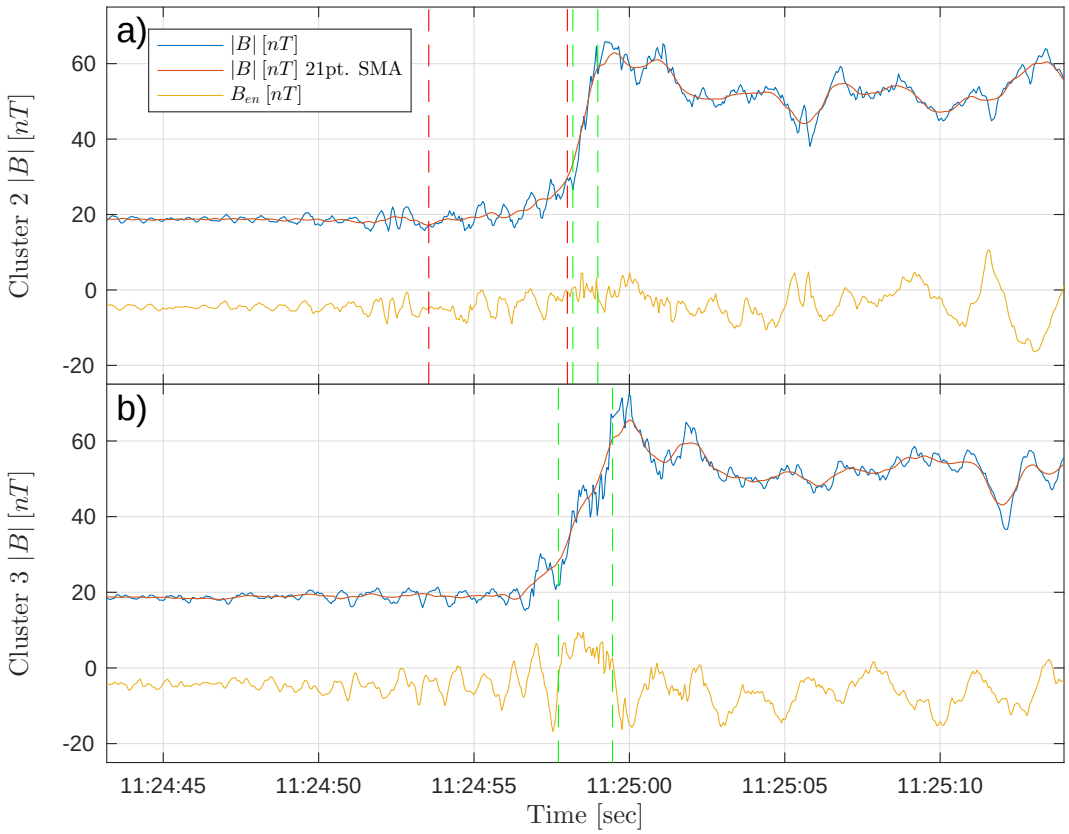

Figure 3.1: Magnetic field intensity plots recorded by Cluster 2 (panel a) and Cluster 3 (panel b) on 9 March 2012. The magnetic field profile of Cluster 3 has been shifted by about 34 sec. The blue line is the measured magnetic field, the red line is the 21-point two sided simple moving average of the magnetic field and the yellow line is the projection of the magnetic field to the normal vector. The vertical dashed red lines (panel a) show the foot identified in the Cluster 2 observations. The vertical dashed green lines show the ramp identified for each spacecraft.

The shock in this example, was observed on 9 March 2012 by Cluster 3 (figure 3.1b) at around 11:24:25 UT and 34 sec later by Cluster 2(figure 3.1a). The Cluster 2 measurements were offset by 34 sec in the plot. The foot observed by Cluster 2 is marked in figure 3.1 (panel a) between the red dashed lines and was traversed in $\Delta t_{ft} = 4.5\, sec$. Table 3.1 summarises important parameters for the two shock observations. The average of the normals determined for each spacecraft was $n_{avg} = [0.78, 0.58, 0.22]$, with an angle between the two normals 12°. From the 34 sec time difference between the two observations and the spacecraft separation along $\mathbf{n_{avg}}$,

Table 3.1: Important parameters, values and calculations for the first example on 9 March 2012 (figure 3.1).

Example 1 : 9 March 2012		
Spacecraft	Cluster 2	Cluster 3
Time of Crossing	11:24:58 UT	11:24:25 UT
$\mathbf{r}$ $[10^3 km]$	$[70.57, -37.29, -31.32]$	$[67.52, -39.94, -23.81]$
$\mathbf{r_d}$ $[10^3 km]$	$[3.05, 2.65, -7.5]$	
Foot Width $[sec]$	4.5	Unclear foot identification
Normal	$[0.89, 0.44, 0.11]$	$[0.64, 0.7, 0.32]$
$< \mathbf{V_u} > [km/sec]$	$[-595.37, 5.46, -63.81]$	
$< \mathbf{B_u} > [nT]$	$[-7.19, 7.43, -15.28]$	$[-6.84, 7.11, -15.52]$
θ_{Vn}	26°	48°
θ_{Bn}	75°	76°
$\theta_{r_d<n>}$	74°	
ω_{ci} $[rad/sec]$	1.8	-

$V_{Sh}^{obs} = 68\, km/sec$ in the spacecraft frame. Along the normal direction calculated from Cluster 2, the spacecraft where the foot was observed (figure 3.1*a*), the two methods estimated $V_{Sh}^{A} = 47\, km/sec$ (31% RE) and $V_{Sh}^{B} = 27\, km/sec$ (60% RE).

3.4.2 Example 2 : 9 Mar. 2012 06:40 UT

The second example is of a shock that was also observed on 9 March 2012 by Cluster 2 at 06:40:11 UT (figure 3.2*a*) and by Cluster 3 at 06:40:44 UT (Figure 3.2*b*). Figure 3.2, follows the same formatting with Figure 3.1. The Cluster 3 time-series was shifted by about 33 *sec*. Using the average MVA normal of the two spacecraft $[0.19, 0.92, -0.34]$, $V_{Sh}^{obs} = 162\, km/sec$.

The foot duration seen by Cluster 2 was 2 *sec* (figure 3.2) and along the Cluster 2 normal $V_{Sh}^{A} = 23\, km/sec$ (86% RE) and $V_{Sh}^{B} = 104\, km/sec$ (36% RE). In this example both spacecraft observed a foot. The foot duration observed by Cluster 3 was 1.3 *sec* and along the normal estimated from the Cluster 3 magnetic field, $V_{Sh}^{A} = 2\, km/sec$ (99% RE) and $V_{Sh}^{B} = 178\, km/sec$ (10% RE).

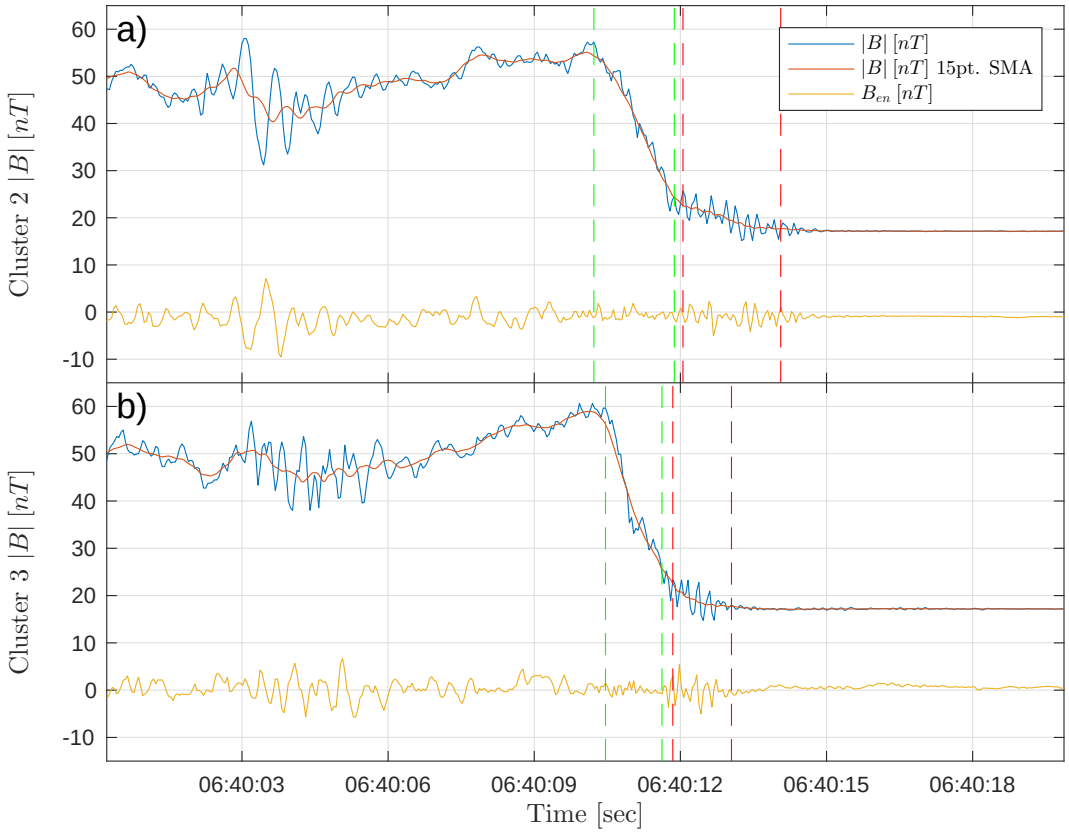

Figure 3.2: Magnetic field intensity plots recorded by Cluster 2 (panel *a*) and Cluster 3 (panel *b*) on 9 March 2012. The magnetic field profile of Cluster 3 has been shifted by about 33 *sec*. The blue line is the measured magnetic field, the red line is the 15-point two sided simple moving average of the magnetic field and the yellow line is the projection of the magnetic field to the normal vector. The vertical dashed red lines show the foot identified only in Cluster 2 (panel *a*) and Cluster 3 (panel *b*) observations. The vertical dashed green lines show the ramp identified for each spacecraft.

Table 3.2: Important parameters, values and calculations for the second example on 9 March 2012 (figure 3.2).

Example 2 : 09 March 2012		
Spacecraft	Cluster 2	Cluster 3
Time of Crossing	06:40:11 UT	06:40:44 UT
$\mathbf{r}$ $[10^3 km]$	$[91.72, -34.55, -49.06]$	$[89.44, -37.64, -42.99]$
$\mathbf{r_d}$ $[10^3 km]$	$[2.28, 3.09, -6.07]$	
Foot Width $[sec]$	2	1.3
MVA Normal	$[0.32, 0.89, -0.33]$	$[0.06, 0.93, -0.36]$
$< \mathbf{V_u} > [km/sec]$	$[-465.49, -0.15, -50.3]$	
$< \mathbf{B_u} > [nT]$	$[-3.89, -4.17, -16.11]$	$[-3.98, -4.43, -16.05]$
θ_{Vn}	73°	89°
θ_{Bn}	89°	85°
$\theta_{r_d n_{avg}}$	42°	
ω_{ci} $[rad/sec]$	1.6	1.6

3.5 Statistical Results and Analysis

In total about 180 crossings of the four Cluster spacecraft were examined, about 720 individual shocks, using the previously mentioned considerations. The majority of the shocks were dismissed due to difficulty distinguishing the foot region ahead of the magnetic ramp. An equally large number of pairs of shocks were dismissed due to disagreement between the normal vectors estimated for each of the spacecraft ($\theta_{n_1 n_2} > 25°$). This resulted in 41 observations.

Figure 3.3 shows the RE of the 41 observations against the angle between the spacecraft separation vector and the average normal vector ($\theta_{r_d n}$). The figure is in essence split in two parts, the measurements where $\theta_{r_d n} < 70°$ and the ones where $\theta_{r_d n} > 70°$. For the sample of the 41 observations, method **A** has an average RE of 153% and a standard deviation of 215%, while method **B** has 113% and 165% respectively. Due to the geometry of the spacecraft separation with the normal vector, it is not clear whether the large RE is caused by error in the measurement of V_{Sh} or due to error of the estimates of the two methods. On the other hand, for $\theta_{r_d n} < 70°$, appear to have a better defined trend on their behaviour. Keeping only the 14 points that have $\theta_{r_d n} < 70°$, the average and standard deviation of the RE are 85% and 10% for method **A** and 41% and 24% for method **B** respectively.

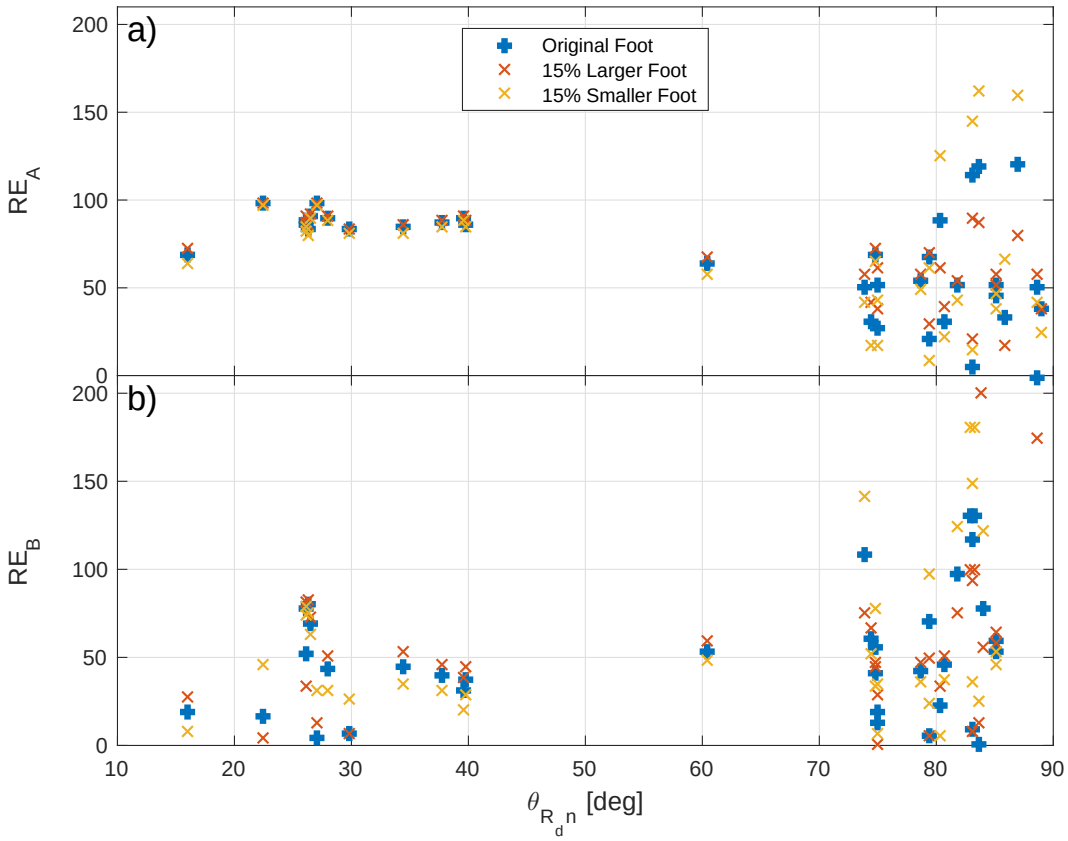

Figure 3.3: RE for for each of the 41 pairs of shock observations by the Cluster spacecraft, against the angle between the spacecraft separation vector and the shock normal direction ($\theta_{r_d n_{avg}}$). Panel (a) shows the RE of the estimates of method **A** and panel (b) those for method **B**. Blue crosses show the RE using the foot as originally identified, the red x-marks show the RE of the same event using a 15% larger foot traversal time and the yellow x-marks for the 15% lower foot traversal time.

In order to take into account the effects of incorrect identification of the exact foot traversal time (Δt_{ft}), the velocities V_{Sh}^{A} and V_{Sh}^{B} were also calculated for a 15% larger and smaller foot traversal time. These estimates are included in order to test the sensitivity of the two methods on the accuracy of the user to identify the correct foot traversal time. In table 3.3, the quantities RE^{O} refers to the RE when the original foot traversal time (as identified by the data) was considered, while RE^{L} and RE^{S} refer to the RE when the larger and smaller times. The absolute difference of the RE from the original, defined as $|\Delta RE^{OL}| = |RE^{O} - RE^{L}|$ (for a larger foot) and $|\Delta RE^{OL}| = |RE^{O} - RE^{L}|$ (for a smaller foot) were also calculated.

The measured V_{Sh} is also plotted against the estimates of both methods in figure

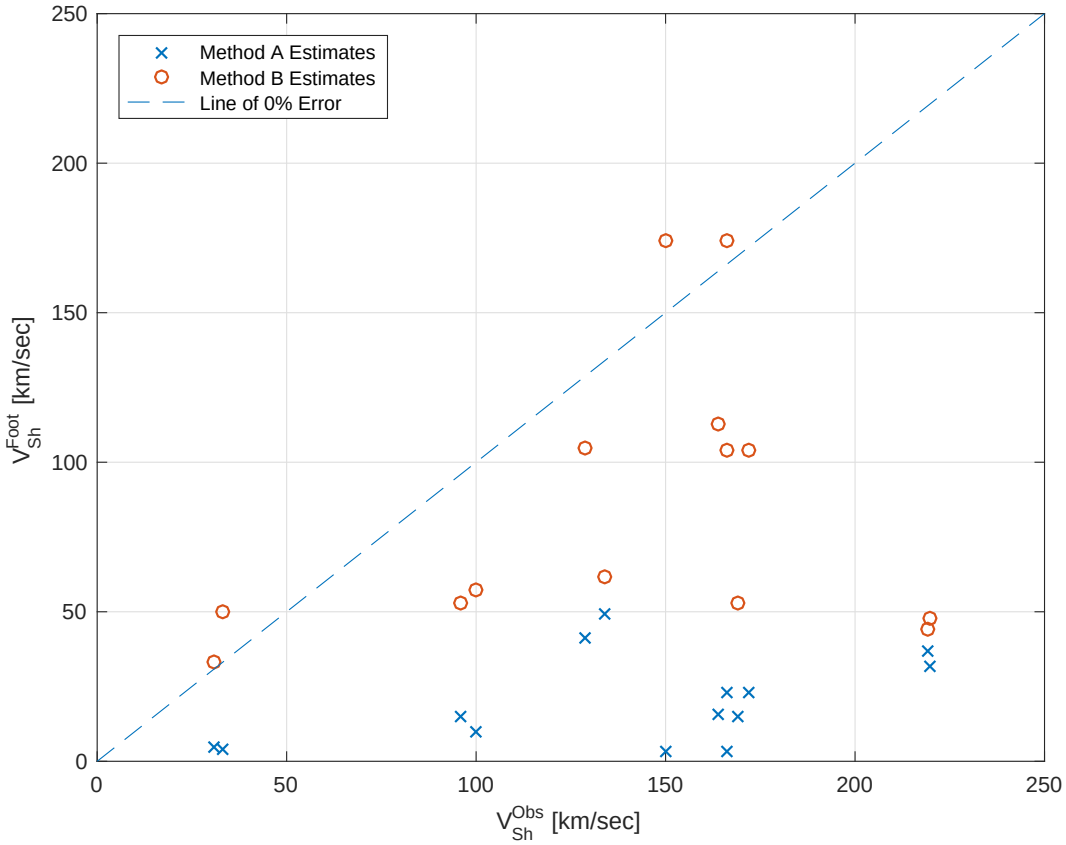

Figure 3.4: Estimated velocity agains measured velocity using two spacecraft measurements for the 14 observations where $\theta_{r_d n} < 70°$. The blue x-marks represent the estimated velocity of method **A** and the orange circles the estimated velocity of the method **B**. The diagonal blue dashed line is is the diagonal for which the estimated velocity is equal to the observed, i.e. if the estimates agreed perfectly with the measured velocity.

3.4, where the blue x-marks show the estimates of method **A** and the red circles the ones of method **B** for the 14 points where $\theta_{r_d n_{avg}} < 70°$. Method **A** underestimates V_{Sh} for all cases substantially. A similar trend can be seen for method **B** as well, but some points are above the line of perfect agreement between observations and estimates.

Method **B** appears to perform better than **A**, although the estimates in the sample have a larger standard deviation. Looking at the estimates using the larger and smaller foot traversal times, method **A** appears to be more stable, but that is not necessarily good. On the contrary, it might indicate a flaw, because the actual traversal time does not appear to be as significant as for method **B**.

Table 3.3: Summary of the mean and standard deviation (SD) of the RE for each of the two methods (**A** and **B**) for all cases of original (RE^O), increased (RE^L) and decreased (RE^S) foot width and the absolute difference of the RE with the increase ($|\Delta RE^{OL}|$) and decrease ($|\Delta RE^{OS}|$) of the foot width for the 14 observations where $\theta_{rdn} < 70°$.

Quantity	RE^O_A	RE^O_B	RE^L_A	RE^L_B	RE^S_A	RE^S_B
Mean	85%	41%	87%	44%	83%	42%
SD	10%	24%	9%	26%	11%	22%

Quantity	$\|\Delta RE^{OL}_A\|$	$\|\Delta RE^{OS}_A\|$	$\|\Delta RE^{OL}_B\|$	$\|\Delta RE^{OS}_B\|$
Mean	1.9%	2.6%	7%	13%
SD	1.3%	1.3%	4.3%	8.8%

3.6 VEX observed shock

Following is one example from an observation of the Venusian bow shock by VEX spacecraft on 05 Nov. 2011 at about 7:00:22 UT. In panel *a* of Figure 3.5 the magnetic field intensity can be seen. The foot region identified is marked between the red dashed line and can be seen that it begins where the upstream waves start to appear and a slight linear increase of the magnetic field magnitude begins to occur. The following three panels of the figure show the projection of the magnetic field vectors in the normal direction ($\mathbf{e_n} = \mathbf{n}$ panel *b*), the vector $\mathbf{e_m} = \mathbf{B_u} \times \mathbf{e_n}$ (*c*) and the vector $\mathbf{e_l} = \mathbf{e_n} \times \mathbf{e_m}$ (*d*).

The direction of the normal vector was determined using MVA of the magnetic field, with eigenvalue rations of 17.7 (maximum to intermediate) and 26.4 (intermediate to minimum). Along with the projection of the magnetic field along the normal vector, which appears constant throughout the ramp region (green vertical lines), the determination of the normal vector is considered to be accurate.

From the VEX measurements, the proton temperature was measured at $T_p \sim 7.5 \cdot 10^5\, K$ and the density at $d_p \sim 6.8\, cm^{-3}$. The ion convective gyroradius was measured at $L_{ci} \sim 242\, km$, the electron inertial length $L_e \sim 2\, km$ and the ion inertial length $L_i \sim 87\, km$.

Table 3.4 summarises the quantities used for the calculation along with the estimate of method **B** for the V_{Sh}, the estimate of the spatial width of the shock ramp (L_r)

Table 3.4: VEX Crossing on 05 Nov. 2011 7:00:22 UT

$< \mathbf{B_u} > [nT]$	$[19.25, -22.86, 27.71]$
$< \mathbf{V_u} > [km/sec]$	$[-882.87, -185.57, -284]$
$\mathbf{n}$	$[0.98, 0.16, 0.14]$
$\omega_{ci}\ [rad/sec]$	3.9
$dt_{foot}\ [sec]$	23
θ_{Bn}	$62°$
θ_{Vn}	$10°$
M_A	2.7
$V_{Sh}\ [km/sec]$	1.4 ± 0.7
$L_r\ [km]$	6.9 ± 2.8
L_r/L_e	3.4 ± 1.4
L_r/L_i	$(7.9 \pm 3.3) \cdot 10^{-2}$
L_r/L_{ci}	$(2.9 \pm 1.2) \cdot 10^{-2}$

and how it compares with L_e, L_i and L_{ci}. The shock is quasi-perpendicular and super-critical, therefore the methods can be applied. The solar wind velocity of this shock is large due to a CME that was observed before the crossing, which leads to a large ion convective gyroradius. The average magnetic field is large, which leads ta a small electron gyroradious.

3.7 Summary

The final set of observations is small in count, compared to the initial number of shock crossings that were considered, but we believe it to be a representative sample for both methods, mainly due to the certainty of the measured V_{Sh} using two spacecraft. The statistical results indicate that neither of the two methods is comparably accurate with the two spacecraft measurements of V_{Sh}. Method **B** [Gosling and Thomsen, 1985] appears to be more accurate in the determination of V_{Sh}, but also has a larger standard deviation, two times larger than method **A** [Moses et al., 1985]. **B** shows a higher sensitivity to the changes of the foot traversal time, which could indicate that the analytical expression that determines the spatial width of the shock foot region is more appropriate, since it does affect the estimate more. This also means that when method **B** is used, greater care must be taken in the identification of the foot traversal time.

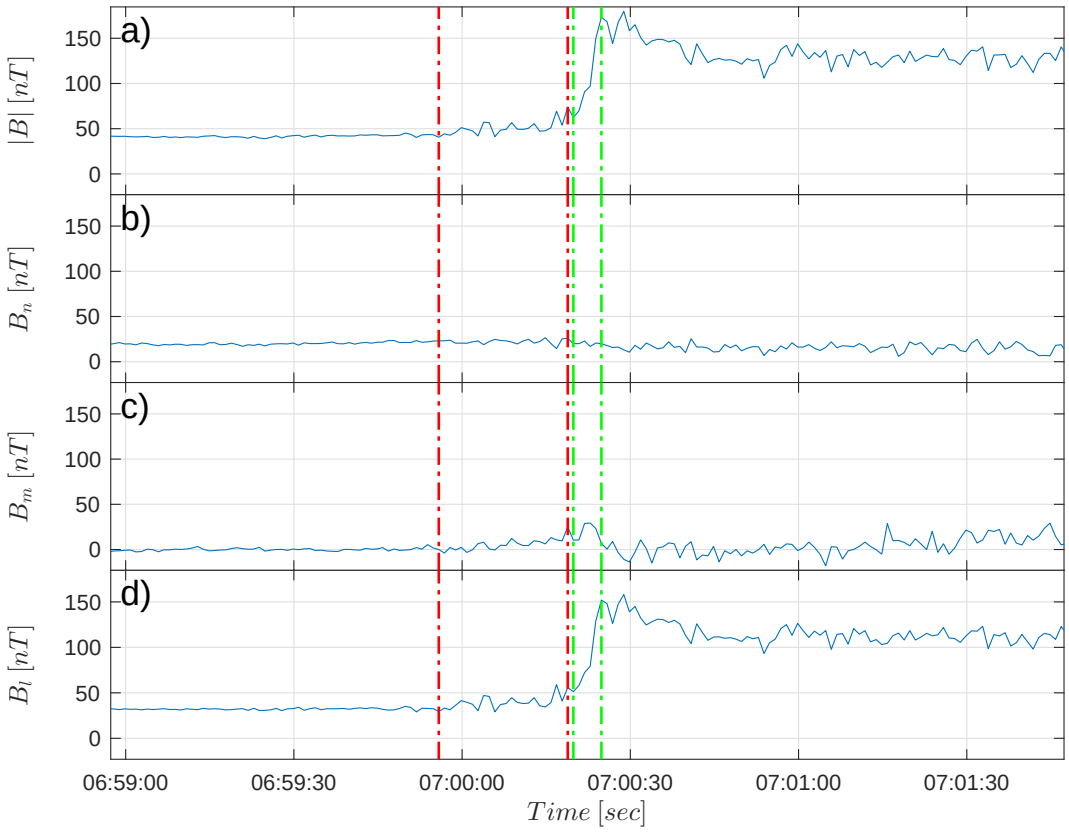

Figure 3.5: VEX Venus Bow Shock crossing on 5 Nov. 2011 around 7:00:22 UT. The ramp (green) and foot (red) regions are marked with dashed vertical lines across all panels. Panel (a) shows the magnetic field intensity. Panel (b) shows the projection of the magnetic field along the normal ($\mathbf{n}$). Panel (c) shows the projection of the magnetic field on the $\mathbf{e_m}$ direction and (d) along the $\mathbf{e_l}$ direction.

Based on the example from the Venusian bow shock, method **B** can be used to determine that the scales of the shock is of the order of $\frac{c}{\omega_{pe}}$.

Chapter 4

Magnetosheath Lion Roars

4.1 Introduction

Packets of short duration (few seconds), right-hand polarized waves, and frequency less than a few hundred Hz, are very common in the magnetosheath, [Smith et al., 1969]. Smith et al. [1969] called this type of emission *lion roars* (LRs) - identified as whistler mode waves - because of their sonified resemblance to male African lion calls. In the majority of studies, the propagation angle relative to the background magnetic field is $\theta_{kB} < 30°$ [Smith and Tsurutani, 1976; Baumjohann et al., 1999; Tsurutani et al., 1982], while Zhang et al. [1998] observed LRs with a much wider range of wave normal angles, some of them, mainly in the vicinity of the bow shock, that were highly oblique. Zhang et al. [1998] also used the evolution of the propagation direction within an interval with LR packets to determine the distance of the spacecraft from the source of the emissions.

Smith and Tsurutani [1976] found a correlation between LR observations and decreases in the magnetic field intensity, accompanied by an increase in particle density. These magnetic field decreases have been linked to mirror-mode structures [Vedenov and Sagdeev, 1961] - the result of an instability where the thermal pressure is anti-correlated with magnetic field fluctuations. Baumjohann et al. [1999] performed a statistical study of LRs associated with mirror modes, using 128 Hz magnetic field measurements from Equator-S. The observations showed a typical frequency range of $[0.05 - 0.15] f_{ce}$. They argued that due to the confinement of the electrons in a

mirror mode, a limit will be imposed on their perpendicular velocity and therefore the region of resonance in the electron velocity space would be limited, compared to the narrow strip shown by Kennel and Petschek [1966] for other cases. The relatively large wave intensities of whistlers, would then lead to electron diffusion towards the parallel velocity direction [Baumjohann et al., 1999]. This would result in a distortion in the contours at the region of resonance similar to the one shown by Kivelson and Southwood [1996]. A case study of LR emissions in mirror-mode structures has been performed by Breuillard et al. [2017], where the properties and dynamics of the waves have been examined. The authors also argue that a statistical study with higher frequency magnetometer data could potentially reveal higher accuracy in the amplitudes of the measurements, compared to the ones provided by Baumjohann et al. [1999].

Tsurutani et al. [1982] concluded that LRs observed close to the magnetopause are generated by the electron cyclotron instability when $T_{\perp e} > T_{||e}$ and a decrease in the magnetic field. The decrease in the magnetic field and the increase of the density, related to the mirror mode, causes the local plasma critical energy ($E_{crit} = B^2/8\pi N$), where N is the density and B the magnetic field, to drop close to the value of the electron thermal energy. When the magnetic field increases, this is no longer true and so the emission terminates. LRs though are not always accompanied by a dip in the magnetic field [e.g. see Zhang et al., 1998]. Kennel and Petschek [1966] showed that the stability of whistler mode waves depends on the electron temperature anisotropy $A_e = T_{\perp e}/T_{||e} - 1$, under the condition $\frac{\omega}{\Omega_{ce}} < \frac{A_e}{A_e+1}$. The growth or damping of the waves, depend also on the resonant frequency of the electrons when compared to the plasma critical energy ($E_r > E_{crit}$). Masood et al. [2006] used this result to show that the majority of the observed magnetosheath LRs in the study originated from a remote region, since there was no correlation with A_e, as LRs existed in all cases where $A_e < 0$, $A_e \sim 0$ and $A_e > 0$. Wilson et al. [2013] showed that when the entire distribution is used, less than half of the observed whistler waves satisfied the instability inequality, while 75% satisfied the inequality when only the halo was considered. Wilson et al. [2013] show an example electron distribution

where they compute A_e for the entire, core and halo components separately. They found $A_e = -0.04$, -0.08, and $+0.25$ for the entire, core, and halo components, respectively. The core and entire components do not satisfy the inequality but the halo does. The reason is that the typical cyclotron energies correspond to the halo, not the core [Wilson et al., 2013].

Using STEREO measurements, Breneman et al. [2010] observed narrowband whistler waves, mainly within stream interaction regions and to a smaller extent, in the vicinity of interplanetary shocks. The authors determined that the emissions had similar characteristics to LRs observed in the magnetosheath. Using the wave parameters observed, Breneman et al. [2010] performed particle tracing simulations which showed a strong interactions of whistler mode waves with halo electrons. The simulations show the largest pitch angle and energy diffusion for a wave normal angle of 45°. The particles used in the simulation were at $100\,eV$ and a 75° pitch angle and the whistlers had a $10\,mVm^{-1}$ amplitude and variety of propagation angles.

4.2 Data

Magnetic field ($\mathbf{B}$) measurements from the MMS search-coil magnetometer (SCM) [Le Contel et al., 2016] were mainly used to identify and study the properties of LRs. SCM measurements were used only during burst mode operation of the spacecraft when $\mathbf{B}$ is sampled at $8192\,Hz$. The sensitivity of the SCM is $\frac{2\,pT}{\sqrt{Hz}}$ at $10\,Hz$, $\frac{0.3\,pT}{\sqrt{Hz}}$ at $100\,Hz$, and $\frac{0.05\,pT}{\sqrt{Hz}}$ at $1\,kHz$. At $1\,kHz$ the resolution is $0.15\,pT$. The SCM data that was used in the study was high-pass filtered at a $10\,Hz$ cut-off frequency. Measurements with amplitude smaller than $5\,pT$ peak-to-peak were also not considered. The quasi-static magnetic field ($\mathbf{B}_0$) was obtained by the fluxgate magnetometer (FGM) [Russell et al., 2016], which provides measurements up to 128 vectors/sec. Particle number density (n) and bulk velocity ($\mathbf{V}_b$) were obtained by the fast plasma investigation (FPI) [Pollock et al., 2016], which can provide measurements of 3D ion and electron distributions at $150\,ms$ and $30\,ms$ time resolution respectively. The electric field $\mathbf{E}$, is measured by the spin-plane double probe (SDP) and the axial double

probe (ADP) instruments on board the MMS [Torbert et al., 2016] and provide the same sampling as $\mathbf{B}_0$. The parameters of the magnetopause Farris et al. [1991] and bow shock [Farris and Russell, 1994] models used in the paper were obtained from Schwartz [1998].

4.3 Methodology

The $\mathbf{B}$ measurements were rotated to the field aligned coordinate (FAC) system, not to be confused with field aligned currents usually denoted as FAC as well. The first coordinate of the FAC system of reference ($\hat{\mathbf{e}}_{||}$) points in the direction of $\mathbf{B}_0$. The second coordinate is defined as $\hat{\mathbf{e}}_{\perp 2} = \hat{\mathbf{e}}_{||} \times \hat{\mathbf{x}}$, where $\hat{\mathbf{x}} = [1, 0, 0]$ (the x direction of the GSE coordinate system). The third coordinate completes the orthogonal basis and is defined as $\hat{\mathbf{e}}_{\perp 1} = \hat{\mathbf{e}}_{\perp 2} \times \hat{\mathbf{e}}_{||}$.

The presence of transverse waves was automatically determined, by looking where the magnitude of $\mathbf{B}_0$ in the $\hat{\mathbf{e}}_{||}$ direction is smaller than the magnitude of $\mathbf{B}_0$ in the $\hat{\mathbf{e}}_{\perp 1}$ and $\hat{\mathbf{e}}_{\perp 2}$ directions. LRs could then be found by looking for a relatively narrow-band peak in the power spectra of the intervals containing transverse waves.

The individual LR intervals were then analysed using a minimum variance analysis (MVA) with adaptive interval selection [e.g., see Wilson III et al., 2017, for discussion]. The software splits the original interval into smaller subintervals which maximize the intermediate to minimum ($\lambda_{int}/\lambda_{min}$) eigenvalue ratio and minimize the maximum to intermediate ($\lambda_{max}/\lambda_{int}$) ratio. In order to achieve that, the original interval is split into smaller overlapping subintervals of variable length and MVA is applied to each of those subintervals. The intervals that are kept are the ones that best satisfy the objectives. In order to ensure the waves that were observed were whistlers and to ensure that they were circularly polarized, only subintervals for which $\lambda_{int}/\lambda_{min} \geq 10$ and $\lambda_{max}/\lambda_{int} < 3$ were kept.

The high sampling frequency of $\mathbf{B}$ allowed for high frequency waves to be observed. This leads to having MVA subintervals that last less than $100ms$. On the other hand, the sampling of $\mathbf{B}_0$, n, and $\mathbf{V}_b$, is considerably smaller. This is why these

quantities were resampled with the sampling rate of **B** using linear interpolation for the points that lie between two actual samples of the three quantities.
For each of the MVA subintervals, the doppler shifted frequency along with the wave number were calculated. In order to obtain the wave number for each of the MVA intervals we follow a similar procedure to that outlined in Wilson et al. [2013]. The cold plasma index of refraction for oblique whistler waves satisfying ${\omega_{rf}}^2 \ll {\omega_{pe}}^2$ and $\omega_{ce} \ll \omega_{pe}$ is given by

$$n^2 = \frac{k^2c^2}{{\omega_{rf}}^2} = \frac{{\omega_{pe}}^2}{\omega_{rf}(\omega_{ce}cos(\theta_{kB}) - \omega_{rf})} \tag{4.1}$$

where ω_{pe} is the electron plasma frequency, ω_{ce} is the electron cyclotron frequency and ω_{rf} is the frequency of the wave in the plasma rest frame. Applying a Doppler shift ($\omega_{sc} = \omega_{rf} - \mathbf{k}\cdot\mathbf{V}_b$) to Equation 4.1 (where ω_{sc} is the frequency observed in the rest frame and $\mathbf{V}_b$ the plasma bulk velocity) leads to the third order polynomial

$$\bar{V}_b\hat{k}^3 + (cos(\theta_{kB}) - \bar{\omega}_{sc})\hat{k}^2 + \bar{V}_b\hat{k} - \bar{\omega}_{sc} = 0 \tag{4.2}$$

where $\hat{k} = kc/\omega_{pe}$, $\bar{V}_b = V_b cos(\theta_{kV})/V_{Ae}$, $\bar{\omega}_{sc} = \omega_{sc}/\omega_{ce}$, $V_{Ae} = B_0/(\mu_0 n_e m_e)^{1/2}$, μ_0 is the free space permeability, n_e is the electron density, and m_e is the electron mass. The real part of the roots of Equation 4.2 provide three solutions for ω_{rf}. Since we are interested in high frequency whistler waves, the valid solutions are the ones where $\omega_{rf} > \omega_{LH}$, where $\omega_{LH} = [(\omega_{ci}\omega_{ce})^{-1} + {\omega_{pi}}^{-2}]^{-1/2}$, $\omega_{pi} = \sqrt{n_i e^2/(m_i\epsilon_0)}$ is the ion plasma frequeny, n_i is the density of ions, B is the magnetic field magnitude, e is the elementary charge, c is the speed of light and m_i and m_e is the mass of the ion and electron respectively.

4.4 Example Lion Roar Measurements

An example of an observed LR is shown in Figure 4.1. Panel *a* shows the measured **B** in FAC, while panel *b* shows the band pass filtered signal of the same interval. The LR was observed by MMS3 on 2015-12-01 at 4:51:00.471 UT and the emission lasted for about 1.6 *sec*. The bandwidth of the filter was determined from the peak

in the power spectra (Fig. 4.1 panels *c*, *d* and *e*) of each of the three components. In this example the frequency band of the emission was identified to be between 45 Hz and 100 Hz and the average peak frequency between the three FAC directions is 69 Hz. The electric field measurements of the interval are also shown in Figure 4.2, which has the same format with Figure 4.1. The peak in the electric field is also within the same bandwidth as in the case of the magnetic field. The combined filtered time-series of the magnetic and electric fields, show that the wave has an electromagnetic nature.

For the LR example in Figures 4.1 and 4.2, the adaptive minimum variance ob-

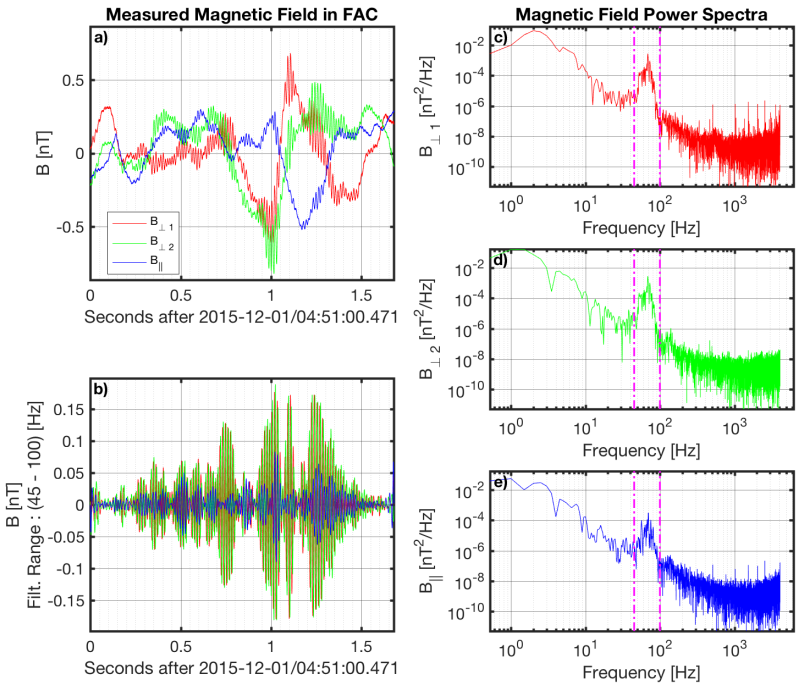

Figure 4.1: Magnetic field measurements of an example Lion roar. The magnetic field in FAC is shown in panel *a*. The band pass ([45-100] Hz) filtered signal of the emission is shown in panel *b*. Panels *c*, *d* and *e* show the power spectrum for each of the three magnetic field components $\mathbf{B}_{\perp 1}$, $\mathbf{B}_{\perp 2}$ and $\mathbf{B}_{||}$ respectively. The vertical magenta lines in panels *c*, *d* and *e* denote the frequency band of the emission as identified by the power spectra.

tained 16 intervals that satisfied the conditions previously described. The measured and band pass filtered $\mathbf{B}$ in GSE coordinates is shown in panel 4.3a, where the x,y and z coordinates are shown in blue, red and yellow respectively. Figures 4.3b-4.3p

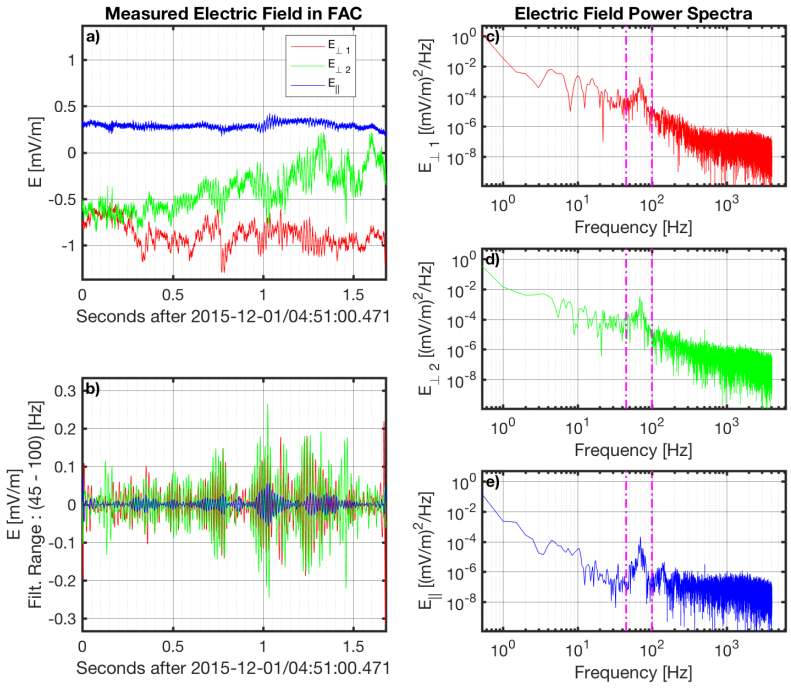

Figure 4.2: Electric field measurements of an example Lion roar. The measured electric field in FAC is shown in panel *a*. The band pass ([45-100] Hz) filtered signal of the emission is shown in panel *b*. Panels *c*, *d* and *e* show the power spectrum for each of the three electric field components $\mathbf{E}_{\perp 1}$, $\mathbf{E}_{\perp 2}$ and $\mathbf{E}_{||}$ respectively. The vertical magenta lines in panels *c*, *d* and *e* denote the frequency band of the emission as identified by the power spectra.

show the magnetic field components in the MVA coordinate basis for that subinterval. The subintervals are shown in Figure 4.3a as the color-coded dashed (start) and dash-dotted (end) vertical lines. One thing that can be noticed in Figure 4.3a is that the subintervals do not cover the entire LR interval that was originally identified. One reason for this is that the eigenvalue ratios were not such as to ensure the good quality of the estimates. Another possible reason is that two subintervals, both with good eigenvalue ratios, but not equal, overlapped for a larger part than allowed, which results in the selection of the best of the two. The method attempts to avoid cross-contamination between multiple frequencies with different propagation properties, but not different modes. All the subintervals may be whistlers but different frequencies may have different θ_{kB}.

Figure 4.4 shows the hodograms of the intervals of Figure 4.3 and each panel of

Figure 4.4 corresponds to the same panel of Figure 4.3 marked with the same letter. For example Figure 4.4k shows the hodogram of the subinterval of Figure 4.3k. The starting point of each hodogram is signified by the green circle and the end by the green cross mark. The direction of the minimum variance eigenvector is shown in the center of each panel, where a dot shows that it is directed outside of the paper, while an x-mark shown that it is directed inside the paper. The blue arrow shows the direction of $\mathbf{B}_0$ projected onto the plane of the maximum and intermediate MVA directions. Figure 4.4a shows the hodogram of the entire time-series on the MVA coordinates calculated for the entire LR interval. What can be seen is that there are parts where the waves are mostly elliptically polarized, but they appear to change orientation, while there are some parts where they might be circularly polarized. On the other hand, the majority of the subintervals in Figures 4.4b-4.4p are almost circularly polarized, with the exception of the subintervals in 4.4b, 4.4n, 4.4o, and 4.4p that are slightly more elliptical. In the subinterval of Figure 4.4c there seems to be some rotation of the ellipse in the three windings as well. Finally the θ_{kB} angle is calculated for each subinterval and is shown for all subplots of Figure 4.4. The average θ_{kB} angle for the 15 subplots is $\sim 20°$. The majority of the subintervals have a θ_{kB} angle which is within one standard deviation (i.e., on the interval [7.8-32.7]°). Calculations for each MVA subinterval shown in Figure 4.3 are provided in Table 4.1. The MVA intervals e, f and j have much more parallel propagation vector to B_0, while interval g propagates in a direction that is more than 45° relative to B_0 and the rest of the MVA intervals have $\theta_{kB} \sim 25°$. On the other hand θ_{kV}, the angle between the propagation vector and the plasma bulk velocity, is more constant for the majority of the intervals $\sim 84° \pm 5$, with the exception of intervals b, d, and g (smallest with $\theta_{kV} = 67°$).

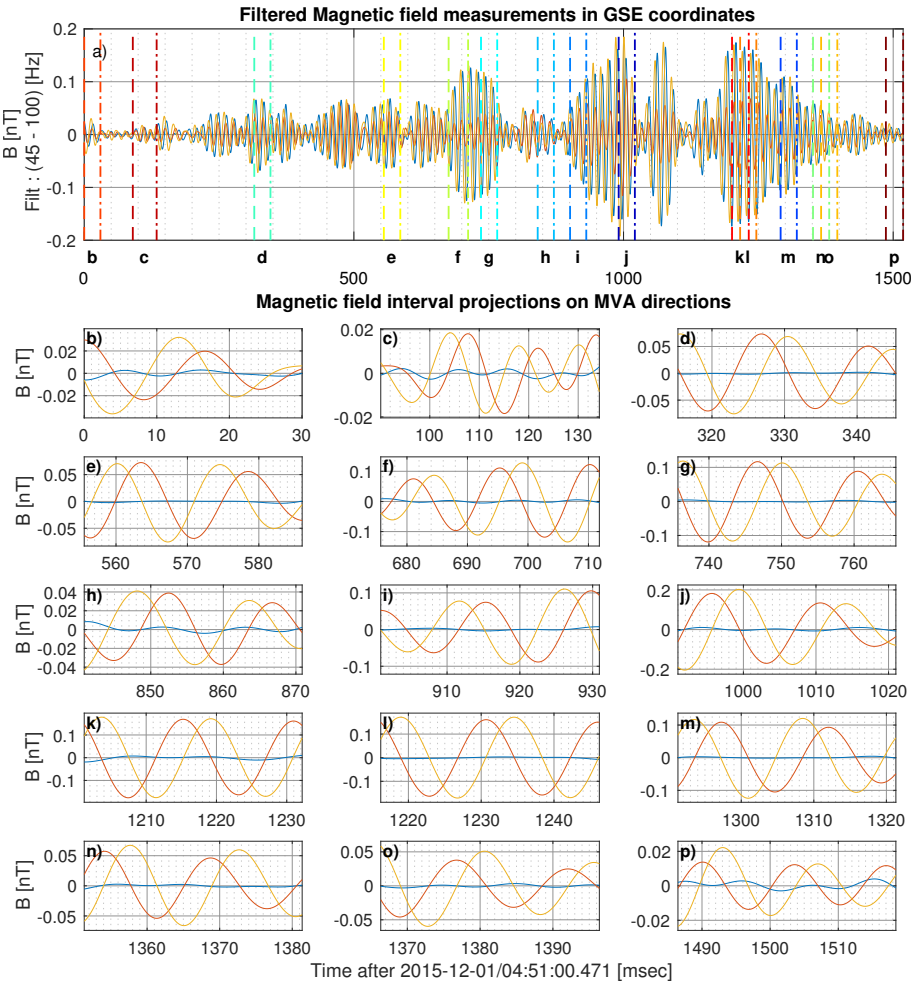

Figure 4.3: Filtered magnetic field measurements in GSE coordinates (a) for the example emission on 2015-12-01. The magnetic field projections on the MVA directions for each interval (b - p). The minimum, intermediate and maximum directions are shown in blue, red and orange, respectively.

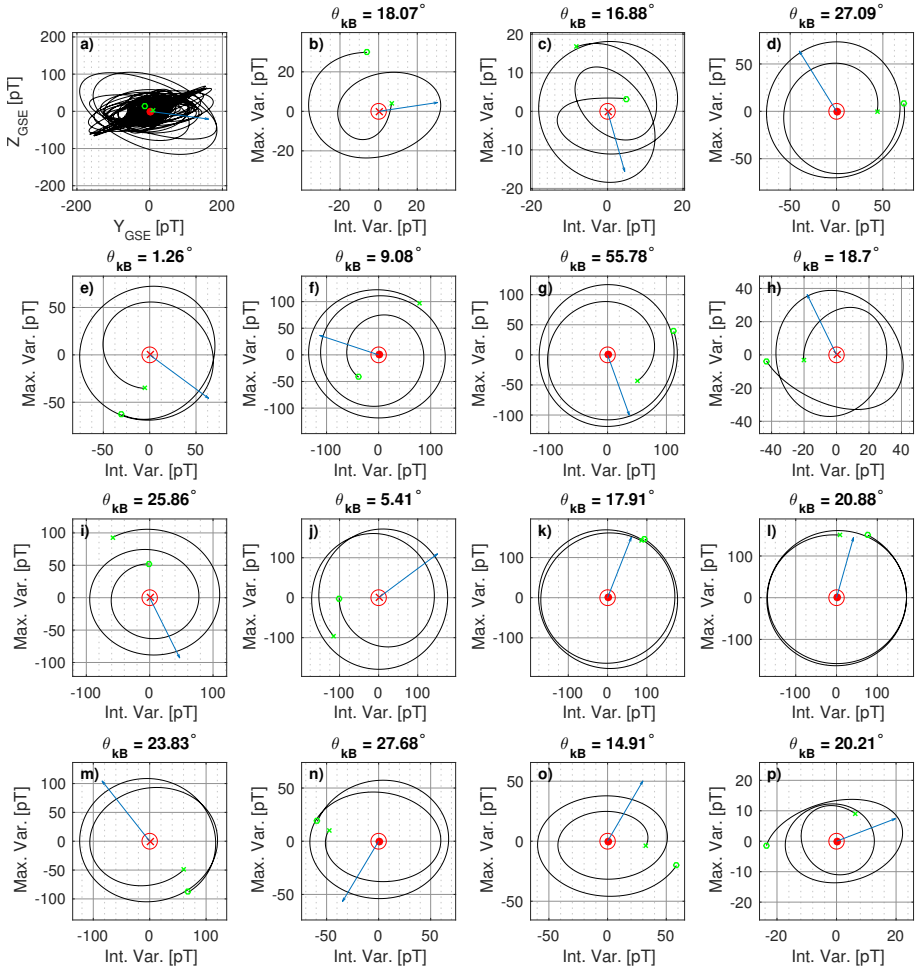

Figure 4.4: Hodograms of the the magnetic field maximum and intermediate components for the individual MVA intervals of the LR example. The blue arrow shows the direction of the background magnetic field ($\mathbf{B}_0$) projected onto the plane of the maximum and intermediate MVA direction. The direction of the minimum variance is shown in the origin of the plots with a dot/cross mark.

Table 4.1: Measurements and Calculations for the intervals of the emission observed on 2015-12-01 at 4:51:00.471 UT by MMS 3.

MVA (Fig. 4.3)	θ_{kB}	θ_{kV}	$\omega_{ce}[Hz]$	$n_e[cm^{-3}]$	$\mathbf{k}$	$\lambda_{max}/\lambda_{int}$	$\lambda_{int}/\lambda_{min}$	$\lambda_{max}/\lambda_{min}$
b	18.1°	77.2°	499.2	19.36	$[0.354, -0.872, 0.339]$	1.5	426.6	622.5
c	16.9°	80.1°	484.8	19.76	$[-0.349, 0.889, -0.296]$	1.1	2011.5	2129.2
d	27.1°	70.7°	489.8	19.75	$[0.444, -0.794, 0.415]$	1.0	1070.3	1099.8
e	1.3°	81.7°	488.3	19.83	$[-0.185, 0.979, -0.090]$	1.1	509.5	546.5
f	9.1°	88.7°	484.5	19.67	$[-0.322, 0.940, -0.112]$	1.1	1439.5	1570.8
g	55.8°	67.0°	488.6	19.75	$[-0.058, -0.534, 0.844]$	1.1	74.5	81.5
h	18.7°	81.9°	489.5	19.73	$[0.515, -0.848, 0.129]$	1.1	408.1	459.8
i	25.9°	85.8°	492.8	19.68	$[-0.540, 0.817, 0.203]$	1.4	387.7	540.0
j	5.4°	88.7°	484.6	19.67	$[0.274, -0.949, 0.153]$	1.0	1549.5	1595.1
k	17.9°	87.7°	486.2	19.66	$[-0.006, 0.935, -0.354]$	1.1	304.2	325.8
l	20.9°	88.1°	487.9	19.52	$[0.029, 0.921, -0.388]$	1.2	1585.9	1901.2
m	23.8°	88.2°	500.4	19.40	$[-0.045, -0.909, 0.413]$	1.4	1241.4	1775.5
n	27.7°	85.8°	508.0	19.20	$[-0.008, -0.855, 0.518]$	1.6	556.7	885.1
o	14.9°	85.2°	517.6	19.13	$[-0.076, 0.953, -0.292]$	1.1	202.4	225.8
p	20.2°	84.8°	520.3	19.04	$[0.002, 0.937, -0.350]$	1.9	61.7	116.0

MVA (Fig. 4.3)	$\mathbf{B}_0\,[nT]$	$\mathbf{V}_b\,[km/sec]$
b	$[-1.56, 17.38, -3.68]$	$[-52.1, -20.5, -45.8]$
c	$[-1.93, 17.01, -2.61]$	$[-47.9, -21.2, -49.0]$
d	$[-2.60, 17.21, -1.84]$	$[-46.0, -22.1, -50.0]$
e	$[-2.86, 17.13, -1.63]$	$[-44.5, -23.4, -49.4]$
f	$[-3.00, 16.99, -1.36]$	$[-44.5, -22.8, -49.5]$
g	$[-3.66, 17.03, -1.12]$	$[-45.1, -22.8, -50.6]$
h	$[-3.89, 17.01, -1.11]$	$[-46.0, -23.7, -52.0]$
i	$[-3.92, 17.12, -1.23]$	$[-46.3, -24.0, -53.1]$
j	$[-3.41, 16.87, -1.85]$	$[-45.6, -23.5, -53.0]$
k	$[-3.94, 16.75, -2.37]$	$[-45.1, -23.7, -53.3]$
l	$[-4.01, 16.79, -2.40]$	$[-45.1, -23.8, -53.4]$
m	$[-4.61, 17.10, -2.44]$	$[-45.5, -24.7, -53.5]$
n	$[-4.93, 17.27, -2.57]$	$[-46.2, -25.6, -53.6]$
o	$[-5.32, 17.51, -2.66]$	$[-46.6, -26.8, -53.5]$
p	$[-5.37, 17.57, -2.81]$	$[-46.5, -27.1, -53.4]$

4.5 Statistical Results

The locations where emissions were detected are shown in Figure 4.5. The magnetopause and bowshock models are also shown in Figure 4.5. A wide range of the magnetosheath x-y plane was sampled, but due to the trajectories of the spacecraft, the sample range of latitudes is not as broad. The location of all the LRs that were observed being closer to the magnetopause, is probably due to the majority of the timing when the satellites were in burst mode operation was set to coincide closer to magnetopause crossings.

The MVA analysis yielded 39709 subintervals from a total of 1738 LR intervals iden-

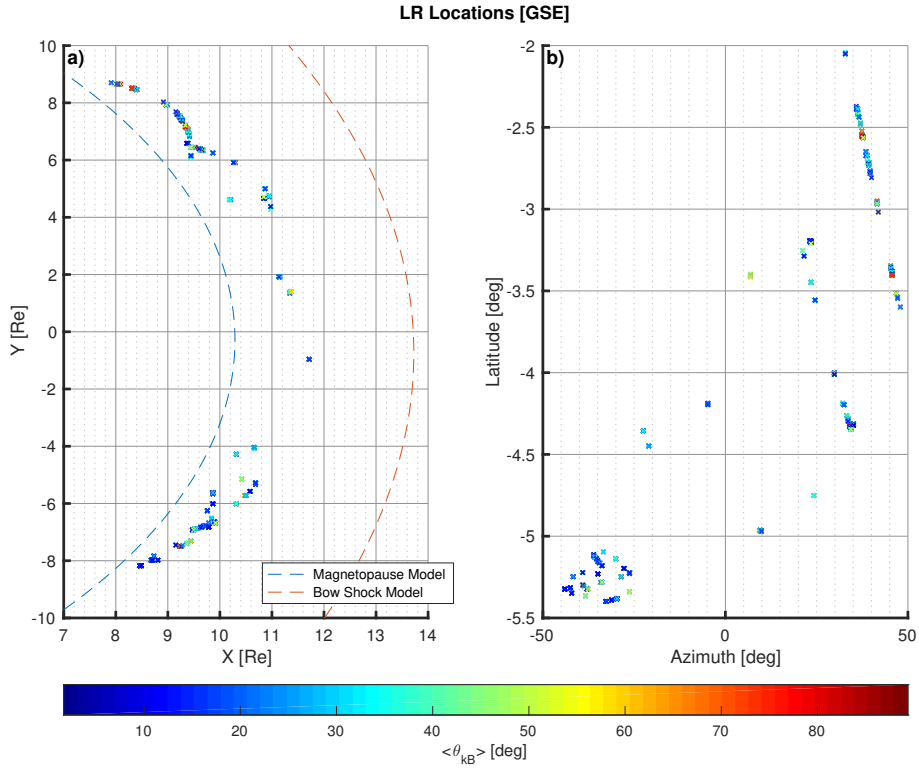

Figure 4.5: Locations of observed LR emissions by the MMS 3 on 18 different dates from 2015-10-16 to 2016-01-13. The 1738 locations shown are the ones where the MVA eigenvalues were considered good. The x-y positions of the spacecraft at the time of observation is shown in panel *a*, along with a model magnetopause (blue dashed line) and model bow shock (red dashed line). In panel *b* the latitude vs the azimuth angle of the position of the observed LR is shown. The points in both panels follow the same colour coding for the angle between the background magnetic field and the average propagation direction of each LR interval observed ($\langle\theta_{\mathbf{kB}_0}\rangle$).

tified, using data from 18 different dates between 2015-10-16 and 2016-01-13. From these MVA subintervals, 2115 were excluded from the study, because the particle density was measured to be $\geq 75\,cm^{-3}$ which is a region where the FPI instrument is inaccurate due to saturation effects. 961 MVA intervals were removed because measurements of the ion and/or electron distributions were not available. The wave properties are summarised in Figures 4.6 - 4.13, where the probability density function (PDF) and the cumulative density function (CDF) that describes the data are overlaid it the figures.

The PDF was fitted to the data, using kernel density estimation defined by

$$f(x) = \frac{1}{nh}\sum_{i=1}^{n} K\left(\frac{x - x_i}{h}\right) \tag{4.3}$$

where n is the number of samples, x_i is each individual sample, K is the kernel function and $h = 1.06\sigma n^{-1/5}$ is generally used as a rule of thumb, with σ being the estimated standard deviation of the sample. For a more detailed explanation of the kernel density estimation see Silverman [1986]. Experimentally determining the PDF of the samples allows then to estimate the cumulative density function ($F(x)$) by integration , as well as obtain the expected value defined by

$$E(x) = \int_{-\infty}^{+\infty} xf(x)dx \tag{4.4}$$

The CDF can then be used to determine the probability $P(x < x_i) = F(x_i) = \int_0^{x_i} f(x)dx$ or inside an interval A, by finding the area of the PDF in that interval. The locations where emissions were detected are shown in Figure 4.5. The magnetopause and bowshock models are also shown in Figure 4.5. A wide range of the magnetosheath x-y plane was sampled, but due to the trajectories of the spacecraft, the sample range of latitudes is not as broad. The location of all the LRs that were observed being closer to the magnetopause, is probably due to the majority of the timing when the satellites were in burst mode operation was set to coincide closer to magnetopause crossings.

Figures 4.6a and 4.6b show histograms of the ratios of the peak frequency over the electron cyclotron ($\omega_{ce} = eB/m_e c$) and the lower hybrid ($\omega_{LH} = ((\omega_{ci}\omega_{ce})^{-1} +$

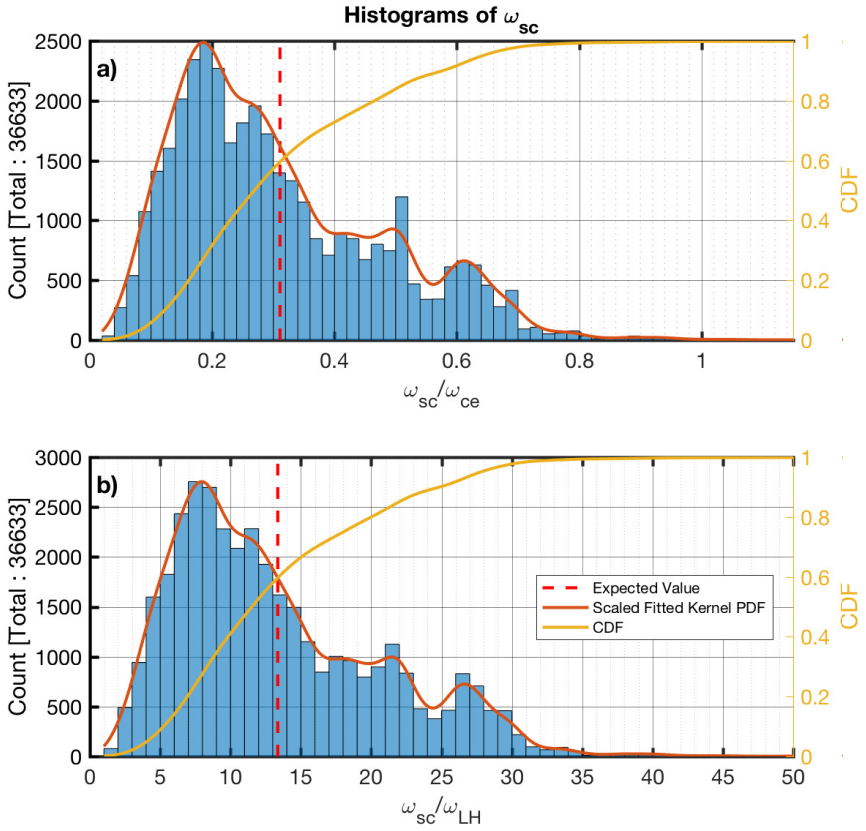

Figure 4.6: Histograms of the ratios of the spacecraft frame frequency peak (ω_{sc}) identified to the electron cyclotron (panel *a*) and the lower hybrid frequency (panel *b*), for each MVA subinterval. The estimated scaled fitted PDF and the CDF are also shown in red and yellow respectively. The calculated average is shown by the dashed vertical red line.

${\omega_{pi}}^{-2})^{-1/2}$) frequency respectively. The estimated PDF is plotted on top of the histograms along with the CDF in panel *b* of both figures.

Figures 4.7a, 4.7b, and 4.7c show the distribution of the MVA subintervals θ_{kB}, θ_{kV} and $\theta_{k\times V\times B}$ angles, where $\theta_{k\times V\times B} = 90° - cos^{-1}(\mathbf{k}\cdot(\mathbf{V}_b \times \mathbf{B}_0))$. The MVA eigenvalue ratio of the intermediate to minimum in Figure 4.8a and the maximum to intermediate directions is shown in Figure 4.8b.

For each of the MVA subintervals, the peak frequency of the emissions in the spacecraft frame, along with plasma measurements, were used with Equation 4.2 to all the MVA results. In total, 30636 of the MVA intervals had $\omega_{rf} > \omega_{LH}$. Figure 4.9 shows the plot of the normalized peak frequency (ω_{rf}/ω_{ce}) against the normal-

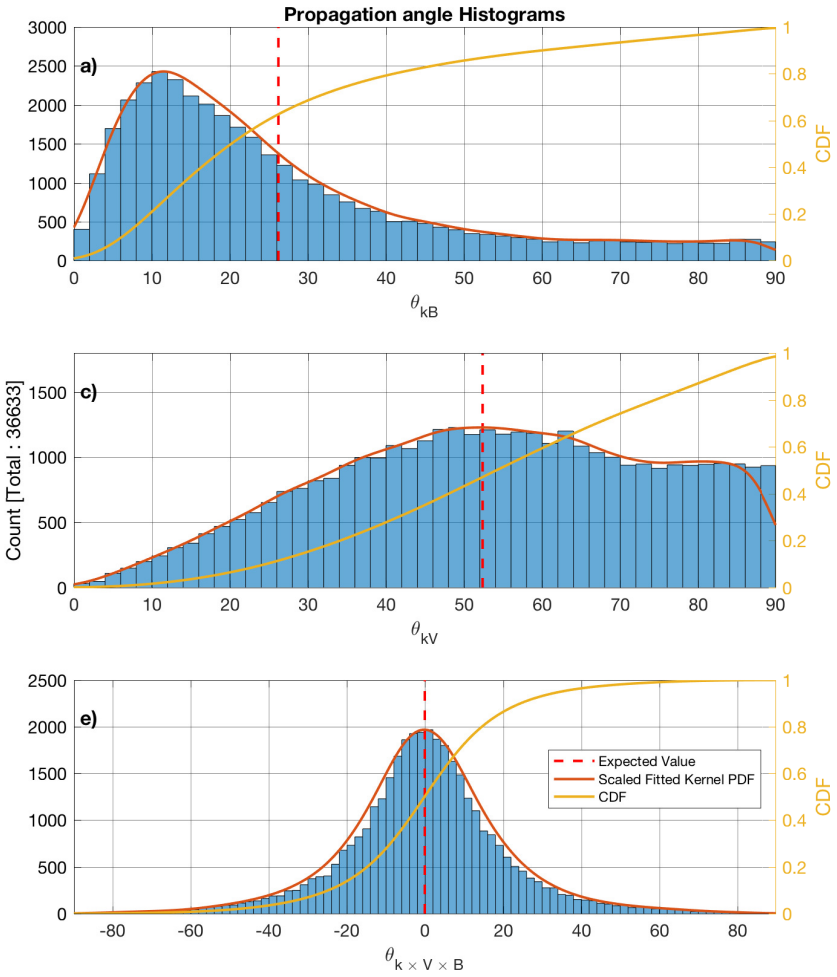

Figure 4.7: Histograms of the propagation vector angle with the background magnetic field (panel a), the plasma bulk flow (panel b) and the latitude from the $\mathbf{V} \times \mathbf{B}$ plane (panel c). The estimated scaled fitted PDF and the CDF are also shown in red and yellow respectively. The calculated average is shown by the dashed vertical red line.

ized wave vector magnitude ($|\hat{k}|$). The histograms for the ratio of the rest frame peak frequency to the electron cyclotron and lower hybrid frequency are shown in Figures 4.10a and 4.10b respectively and the formatting is the same as the previous histogram figures.

The histograms of the angles θ_{kB}, θ_{kV} and $\theta_{k \times V \times B}$ for the 30636 MVA subintervals for which the rest frame frequency adheres to the condition $\omega_{rf} > \omega_{LH}$ are shown in

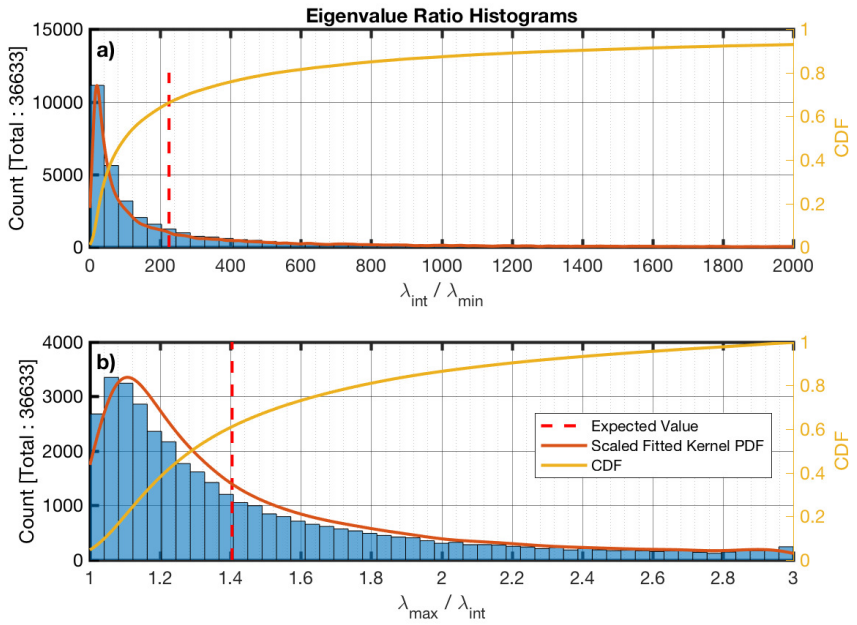

Figure 4.8: Histograms of the eigenvalue ratios of the intermediate to minimum (panel *a*) and the maximum to intermediate (panel *b*) MVA components. The estimated scaled fitted PDF and the CDF are also shown in red and yellow respectively. The calculated average is shown by the dashed vertical red line.

Figures 4.11a, 4.11b and 4.11c respectively.

A histogram of the magnetic field amplitude in the maximum MVA coordinate ($\mathbf{B}_{max}$) is shown in Figure 4.12 for the subintervals where Equation 4.2 had a valid solution. In this case the PDF was estimated for the actual data and not the logarithm of the data, which is shown in the plot for convenience. The amplitude of the same subintervals is plotted relative to the θ_{kV} angle in Figure 4.13. Figures 4.13a - 4.13i show the plots of θ_{kV} against the maximum amplitude of the same subintervals from Figure 4.12 with each panel showing the subintervals within the θ_{kB} as indicated in the figures. The histograms of the plasma beta for the electrons and the ions for the 28983 MVA results for which $\omega_{rf} > \omega_{LH}$ is true, are shown in Figures 4.14a and 4.14b. In both figures the x axis has been limited and the maximum value for each case is indicated. In the case of electrons, the number of subintervals where $\beta_e > 7$ is 16 and in the case of the ions, there are 1289 subintervals with $\beta_i > 20$.

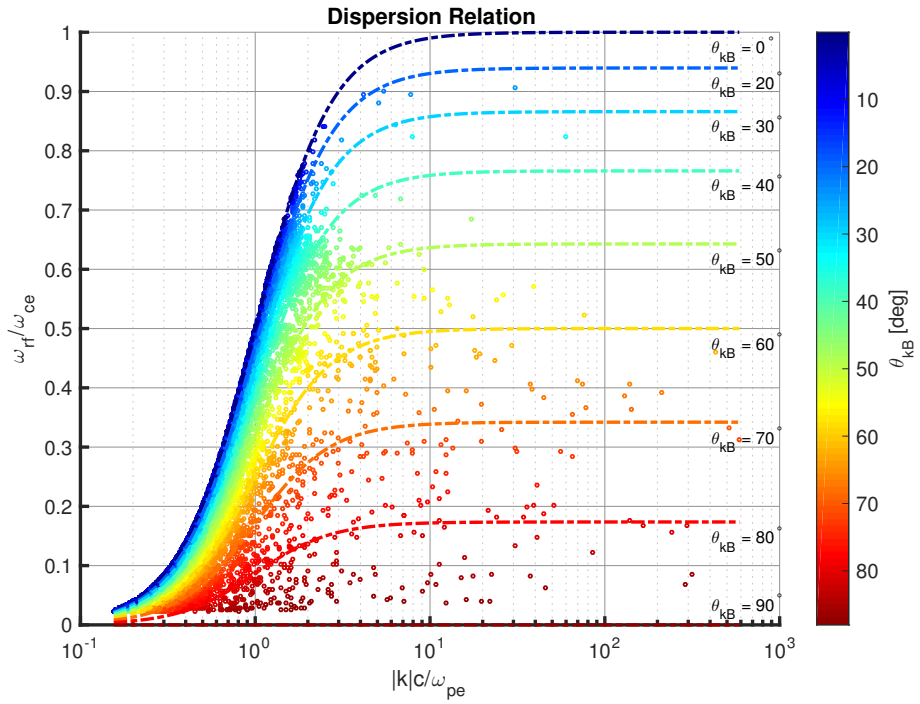

Figure 4.9: Dispersion relation for the 30636 MVA intervals where $\omega_{rf} > \omega_{LH}$. The circles are the points of the individual MVA subintervals. The dashed lines show the calculated dispersion for a given θ_{kB} angle.

4.6 Discussion

In this chapter the properties of circularly polarized electromagnetic waves in the magnetosheath were examined based on 36633 subintervals of 1738 intervals of magnetic field measurements from the MMS identified as lion roar emissions. The 1738 intervals were automatically identified based on the magnetic field measurements with the main constraint that they are primarily transverse waves. The frequency band of the lion roars in each interval was manually identified based on the power spectrum of the magnetic field of the intervals. The intervals were then submitted to an automatic adaptive interval algorithm that uses MVA to identify appropriate subintervals. From all the MVA subintervals, only the ones that were circularly polarized and had adequately large eigenvalue ratios, to ensure high accuracy in the estimation of **k**, were kept. Using the the cold plasma index of refraction for oblique whistler waves along with the Doppler shift we obtained ω_{rf} and $|k|$ for each MVA subinterval. From the original subintervals, 28983 satisfied $\omega_{rf} > \omega_{LH}$ and they were

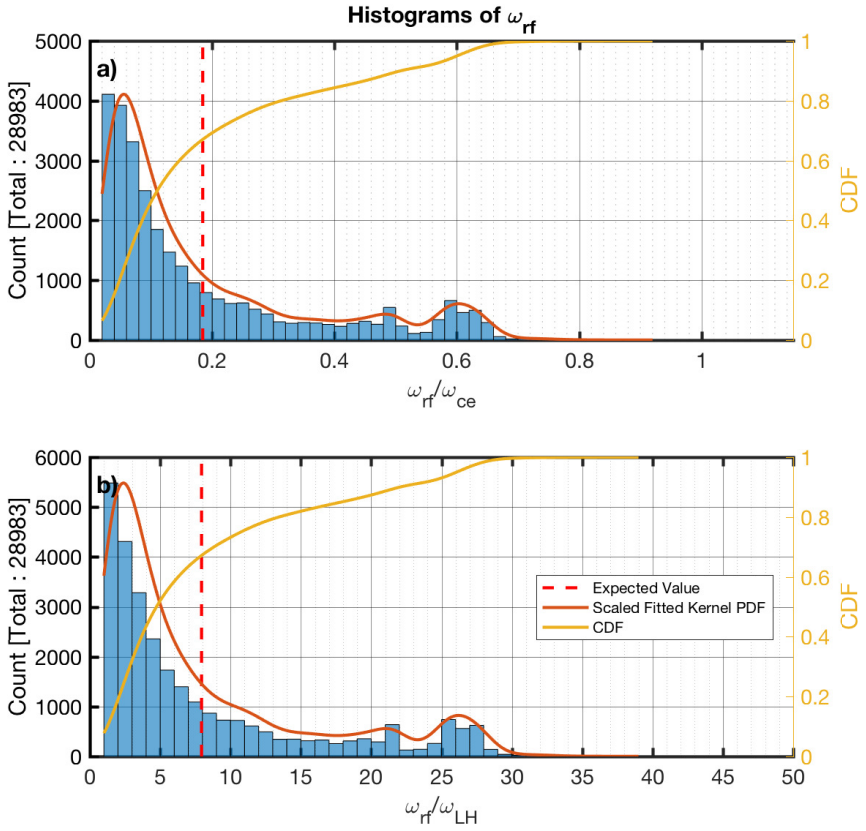

Figure 4.10: Histograms of the ratios of the rest frame frequency peak (ω_{rf}) identified to the electron cyclotron (panel a) and the lower hybrid frequency (panel b), for each MVA subinterval. The estimated scaled fitted PDF and the CDF are also shown in red and yellow respectively. The calculated average is shown by the dashed vertical red line.

further examined. No obvious correlation could be found between the coefficients of Equation 4.2 and the lack of a solution that satisfied $\omega_{rf} > \omega_{LH}$ for the other 7650. From the dispersion relation plot in Figure 4.9, we can see that the frequency-wavenumber plane has been well sampled for all propagation directions up to $\sim 2.4kc/\omega_{pe}$. For wavenumbers $> 2.4kc/\omega_{pe}$ there are more samples for waves that propagate at $\theta_{kB} > 40°$.

The plasma beta for the ions (Fig. 4.14b) has $E(\beta_i) \sim 9.6$ and the histogram peaks at around 1.4 and 12. For the electrons (Fig. 4.14a), $E(\beta_e) \sim 1.2$ and 98% of measurements are < 4.

The majority of the emissions (99.8%) have $\omega_{sc} < \omega_{ce}$ (Figure 4.6a) and (99.7%)

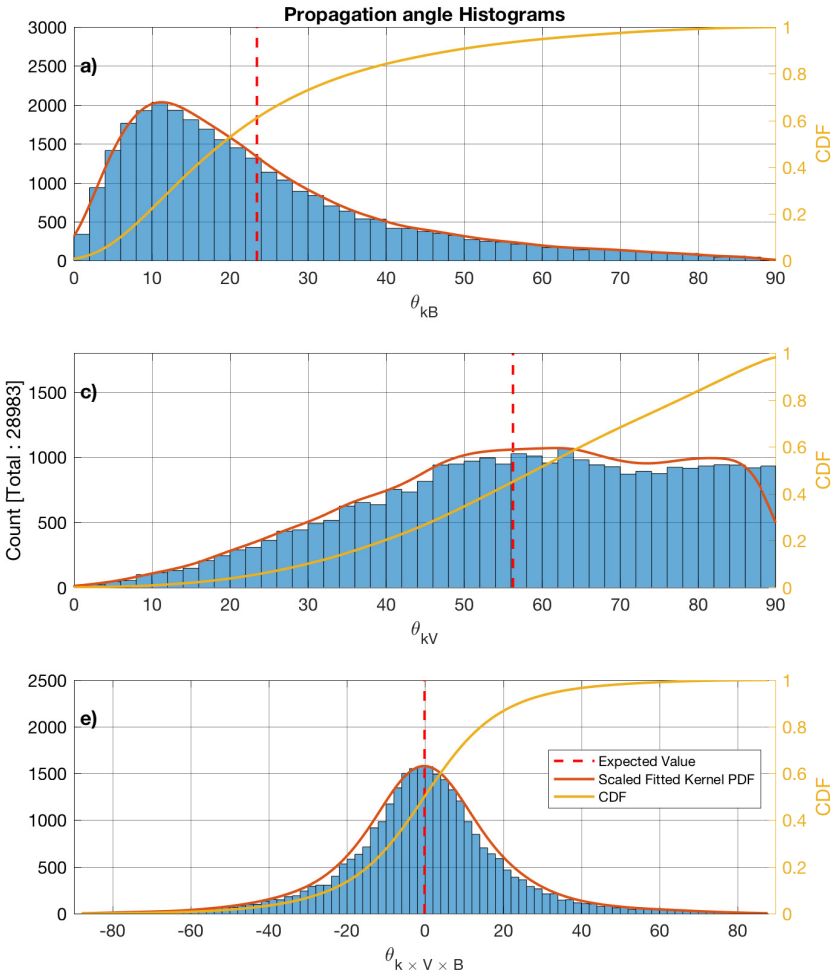

Figure 4.11: Histograms of the propagation vector angle with the background magnetic field (panel *a*), the plasma bulk flow (panel *b*) and the latitude from the $\mathbf{V} \times \mathbf{B}$ plane (panel *c*) for the MVA subintervals for which $\omega_{rf} > \omega_{LH}$. The estimated scaled fitted PDF and the CDF are also shown in red and yellow respectively. The calculated average is shown by the dashed vertical red line.

$\omega_{LH} < \omega_{sc} < 48\omega_{LH}$ (Figure 4.6b). Based on the PDF of ω_{sc}/ω_{ce} and ω_{sc}/ω_{LH}, the distribution has three peaks, the first one being substantially larger, at $\sim 0.19\omega_{ce}$ ($\sim 8.1\omega_{LH}$), $\sim 0.49\omega_{ce}$ ($\sim 21\omega_{LH}$), and $\sim 0.61\omega_{ce}$ ($\sim 27\omega_{LH}$). The average (Expected value shown in Equation 4.4) frequency is $0.3\omega_{ce}$ and $13.4\omega_{LH}$. In the plasma rest frame, we observe that the distributions have been shifted to lower frequencies and the majority of the subintervals (98%) have $\omega_{rf} < 0.72\omega_{ce}$ (Figure 4.10a) and (92%)

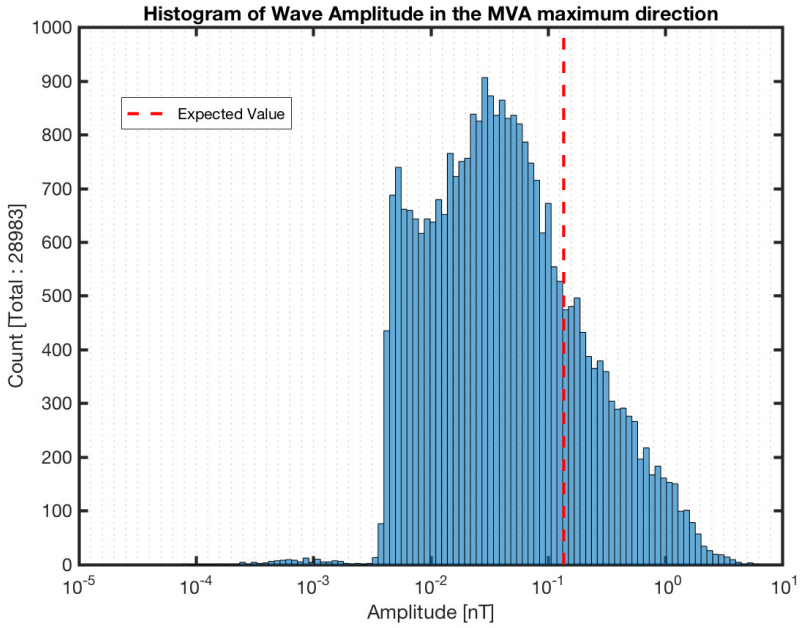

Figure 4.12: Histogram of the amplitude in the maximum MVA coordinate of the MVA subintervals where $\omega_{rf} > \omega_{LH}$. The expected value obtained by the PDF fitted to the data is shown. The fitted PDF is not shown because it was not estimated for the logarithm of the data.

$\omega_{LH} < \omega_{rf} < 30\omega_{LH}$ (Figure 4.10b). The shape of the distributions has also changed significantly. The peak at $\sim 0.61\omega_{ce}$ ($\sim 27\omega_{LH}$) still appears with a similar magnitude, but the distribution left of this point now resembles more an exponential decay, with a peak at $\sim 0.06\omega_{ce}$ ($\sim 2.4\omega_{LH}$). The average value of ω_{rf} is $\sim 0.18\omega_{ce}$ ($7.9\omega_{LH}$). The average frequency in the rest frame is about half of that in the spacecraft frame.

The minor differences that are seen between the pairs of Figures 4.7a and 4.11a, 4.7b and 4.11b, and 4.7c and 4.11c are due to the exclusion of some subintervals because no valid solutions could be found for Equation 4.2. Comparing the histograms of the θ_{kB} angle between the subintervals in the spacecraft frame (Figure 4.7a) and the doppler shifted results (Figure 4.11a), the subintervals with $\theta_{kB} \sim 90°$ are not present and the transition from 60° to 90° has a negative slope, while in Figure 4.7a it appears to be more flat. Similarly, the histogram of the θ_{kV} angle of the subintervals in the spacecraft frame (Figure 4.7b) appears to peak $\sim 50°$, which is not

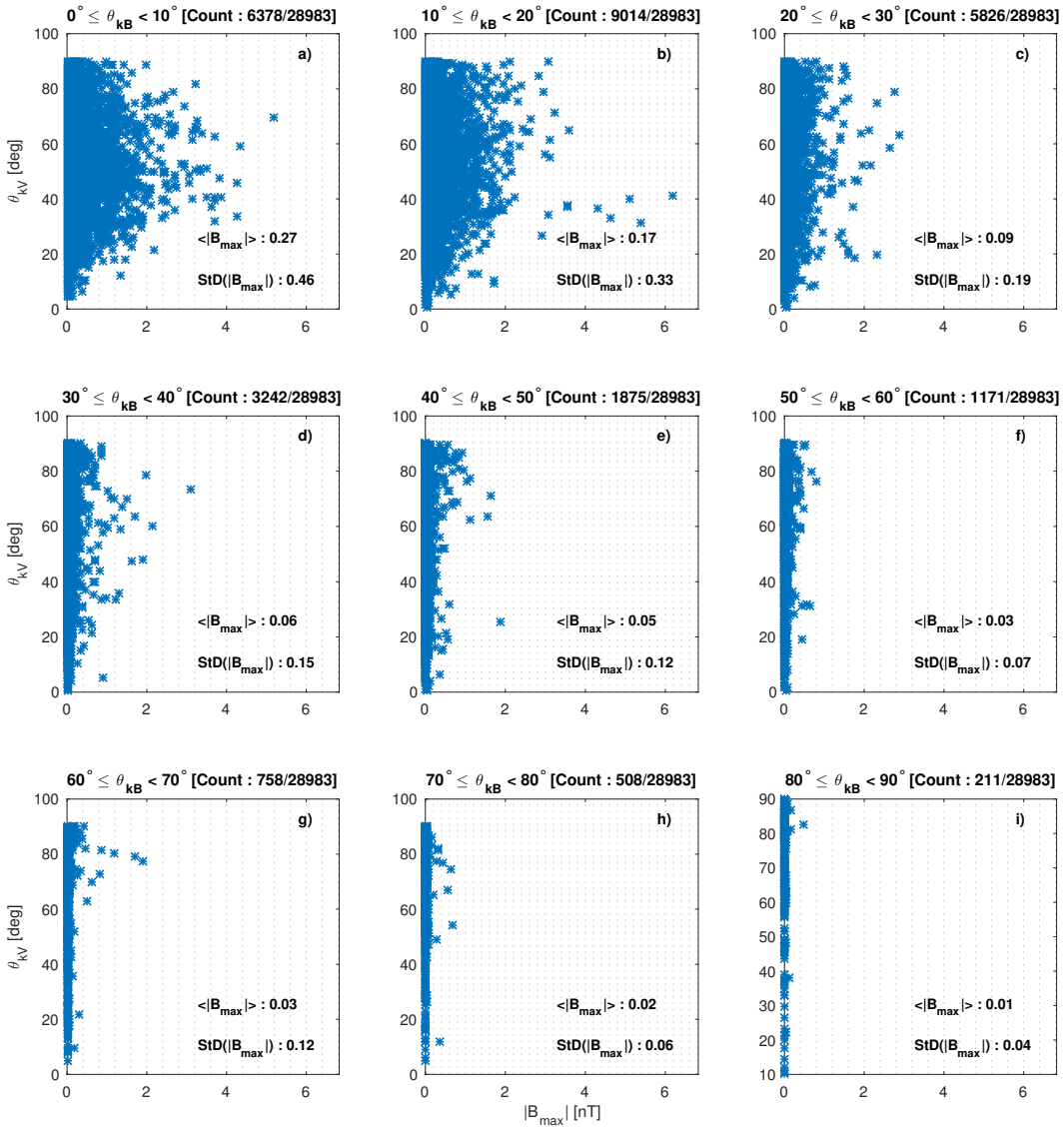

Figure 4.13: Plots of θ_{kV} against the amplitude in the maximum MVA coordinate of the MVA subintervals where $\omega_{rf} > \omega_{LH}$. In each panel emissions with the θ_{kB} range are shown. The mean ($< |\mathbf{B}_{max}| >$) and the standard deviation ($StD(|\mathbf{B}_{max}|)$) for each interval of θ_{kB} is also shown.

observed in the Doppler shifted results (Figure 4.11b). The shape of the histograms for the $\theta_{k\times V\times B}$ (Figures 4.7c and 4.11c) is similar in both cases.

From the estimated PDFs for all the MVA subintervals (Figure 4.7a, 4.7b and 4.7c), the expected values are $E(\theta_{kB}) = 26°$, $E(\theta_{kV}) = 52°$ and $E(\theta_{k\times V\times B}) \sim 0°$, while 81% of the samples have $\theta_{kB} < 45°$, $\theta_{kV} > 32°$, and $-26° < \theta_{k\times V\times B} < 26°$. When considering the valid Doppler shifted only subintervals, the expected values are

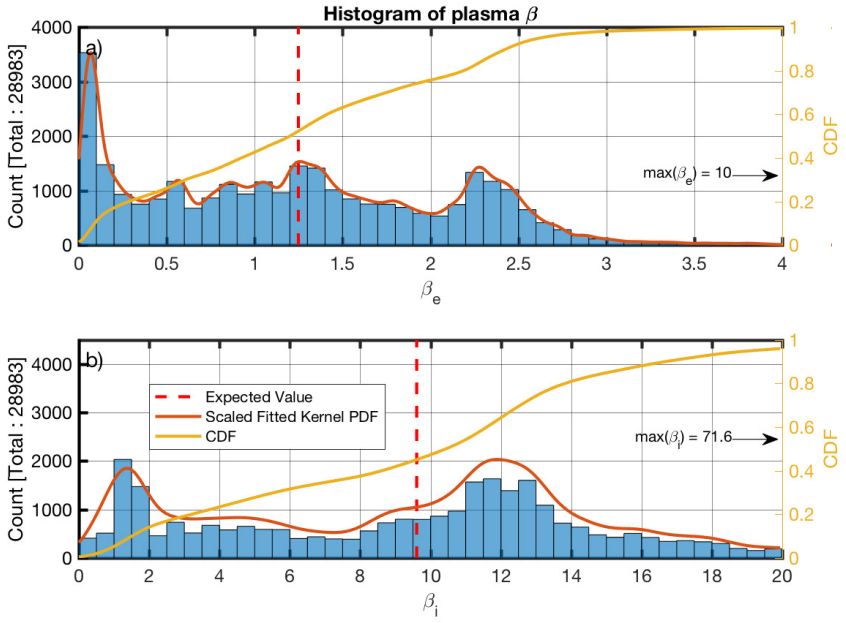

Figure 4.14: Histograms of the calculated plasma beta for the electrons (panel *a*) and ions (panel *b*) for the MVA subintervals for which $\omega_{rf} > \omega_{LH}$. The estimated scaled fitted PDF and the CDF are also shown in red and yellow respectively. The calculated average is shown by the dashed vertical red line.

$E(\theta_{kB}) = 23°$, $E(\theta_{kV}) = 56°$ and $E(\theta_{k\times V\times B}) \sim 0°$ and 81% of the samples have $\theta_{kB} < 38°$, $\theta_{kV} > 37°$, and $-26° < \theta_{k\times V\times B} < 26°$.

The majority of LRs propagate obliquely relative to the plasma bulk flow and are more likely to be observed to propagate close to parallel to the background magnetic field. The average value of $\theta_{k\times V\times B} \sim 0°$ could indicate that the free energy source for the waves is mainly linked to the magnetic field and the plasma bulk flow. The peak that was observed at $\theta_{kV} \sim 50°$ is consistent with the results of Wilson et al. [2013], where they argued that the lower sampling frequencies were the reason that waves with lower θ_{kV} were not observed due to a Doppler shift above the Nyquist frequency. On the other hand, the data used in this study were sampled at much higher frequency and the same phenomenon is observed.

The majority of the studies have observed few cases of LRs with $\theta_{kV} < 45°$. Wilson et al. [2013] reported no observations of whistler waves with such angles, Moullard et al. [1998] reported an average 70° and from the examples of Zhang et al. [1998] we

found two cases with $\theta_{kV} < 45°$ from the examples presented in the paper. In this study $\sim 35\%$ of the MVA subintervals have $\theta_{kV} < 45°$ and $\sim 27\%$ of the Doppler shifted MVA subintervals. The difference results from an inability to calculate the Doppler shift for all MVA subintervals, because there was no solution that solved Equation 4.2 and satisfied the conditions previously mentioned.

Looking at Figures 4.6a and 4.6b, and 4.10a and 4.10b, it can be seen that the shapes of the distributions of ω/ω_{ce} and ω/ω_{LH} both in the spacecraft and the plasma rest frame are similar and the scaling between them is $\sim \sqrt{m_i/m_e}$. This is because the ion plasma frequency of all measurements is very high. This makes the lower hybrid frequency dependant upon ω_{ci} and ω_{ce}. More specifically $(\omega_{ce}/\omega_{LH})^2 \sim {\omega_{ce}}^2/(\omega_{ce}\omega_{ci}) = m_i/m_e$. Assuming that $n_e \sim n_i$ then $\omega_{pe} > \omega_{pi}$ and so the condition for the waves satisfy $\omega_{ce} \ll \omega_{pe}$, required by Equation 4.1.

The expected value for the maximum MVA component peak amplitude of the emissions was found to be $\sim 0.14\,nT$, while 77% of the samples have an amplitude $< 1\,nT$. The maximum amplitude found was $\sim 6.2\,nT$. Based on Figures 4.13a - 4.13i, the largest amplitude emissions were observed for smaller θ_{kB} angles, For angles $\theta_{kB} < 60°$, it appears that the amplitudes have a larger mean and standard deviation than in the cases where $\theta_{kB} \geq 60°$. Finally for $\theta_{kB} < 80$, the amplitude has a smaller range for smaller angles of θ_{kV}.

4.7 Summary

The source of LRs in the magnetosheath is most likely a temperature anisotropy of the halo electrons. This anisotropy can in some cases be related to mirror modes, often observed in the magnetosheath. Lengyel-Frey et al. [1994] have calculated the energies for the resonant electrons for each of the cases of Landau damping, cyclotron resonance, and anomalous cyclotron resonance due to the interaction with whistler waves observed at interplanetary shocks. The lower energy electrons experience Landau interactions, and the higher energy electrons experience cyclotron

interactions. LRs in the magnetosheath will affect the electron distribution similarly since they are oblique and observed at a high range of frequencies. Landau damping will result in a more oblate electron velocity distributions in the direction of the background magnetic field. Cyclotron interactions can cause a temperature anisotropy in the halo electrons. If the interaction results in damping of the wave, then it will increase the temperature in the perpendicular direction relative to the background magnetic field [Brice, 1964]. The interaction between the waves and the electrons can lead to a distribution different than the one that generated the waves [Chang et al., 2013; Hughes et al., 2014].

As LRs propagate from the bow shock towards the magnetopause, they play an important role in the regulation of the halo electron anisotropies in the magnetosheath. They also seem to be closely related to mirror mode structures and the regulation of the temperature distribution of the trapped electrons in these structures [Breuillard et al., 2017]. Quasi-linear and nonlinear particle-wave interactions could lead to un-trapping electrons from the mirror mode. The sampling rate and the quality of the MMS instruments could offer better insight on the mechanisms that generate LRs and how they affect the plasma as they propagate.

Finally, whistler mode waves have been observed in many different regions of the heliosphere, such as magnetic clouds [Moullard et al., 2001], planetary atmospheres [Hughes et al., 2014] and they are closely linked to collisionless shocks, planetary and interplanetary [Gary and Mellott, 1985; Lengyel-Frey et al., 1994; Walker et al., 1999]. It is important to understand their properties, generation mechanisms and the effects they have in the plasma in order to extrapolate to inaccessible regions of space.

Chapter 5

Conclusions and Further Research

The interaction of the solar wind with the Earth's magnetic dipole can provide useful insight to the fundamental physics of plasma. The system that forms the magnetic field environment of the Earth consists of many distinct regions that interact with each other and their states are linked.

Part of this system is the bow shock, which heats the incoming solar wind and reflects particles, depending of the geometry of the shock and the type of the shock. The discrimination of the types of collisionless shocks depends on several parameters. Some of these parameters are the Mach number and the shock normal angle. What determines the underlying physics of the shocks is the dissipation scale of the shock, which in turn is determined by the spatial scales of the shock.

Single spacecraft missions are being planned for the observation of phenomena within our solar system. The data obtained by single spacecraft missions are very useful, but in order to be interpreted, they need to be complemented by analytical methods. The analytical methods that are used are based on various assumptions, in order to be simplified and easily applied. Understanding the limitations of these methods is important.

In Chpater 3 two such methods were examined and their estimates were verified by two-spacecraft observations. Both methods use the same basis to form a mathematical expression that determines the velocity of the shock. This common element is the region in front of the shock that is named *foot*. The difference between the two methods is mainly due to assumption that oversimplified the problem, in the first

case, and a more rigorous approach by the second one. From the results it can be seen that the assumptions lead to a large deviation between the estimates of the two methods.

The statistical study also provided error margin that can be used in future missions that consist of a single spacecraft. Along with other data they can prove very beneficial in studies of the magnetic environments of other planets.

Downstream of the bow shock is the magnetosheath, a region where turbulence and plasma waves can be observed on every satellite traversal. One of the commonly occurring emissions that can often be observed by in-situ measurements are whistler waves: right-handed circularly polarized waves, most likely originating by a temperature anisotropy of halo electrons. When observed in the magnetosheath, whistler waves were originally named lion roars and so in many cases they are still referred to with this name. Lion roars can interact with the particles and affect their distributions because of their oblique propagations at high frequencies.

In Chapter 4 a relatively large number of lion roar observations in the Earth's magnetosheath were presented. The data, obtained by the MMS, offer a large sampling rate when compared to previous missions. This allowed the application of filtering and adaptive minimum variance to magnetic field measurements. That would be much harder with a lower sampling rate, since the MVA would not give adequate eigenvalue ratios for an accurate estimation. The adaptive MVA allowed a more detailed determination of the propagation direction of the observed emissions.

The detailed probability distributions of the observed measurements can provide insight into the properties of lion roars. In a future study it would be beneficial to examine the particle velocity distributions, which are also available for the dates that where selected in the samples of Chapter 4. By examining the particle distributions, along with the results of this work could provide insight into the generation mechanism of lion roars.

Another possible study would be to examine how often the emissions are associated with magnetic mirrors. These magnetic structures are also often observed in the Earth's magnetosheath and there are evidence that when they appear, the neces-

sary conditions for the generation and propagation of lion roars are satisfied.

References

Bale, S. D., Balikhin, M. A., Horbury, T. S., Krasnoselskikh, V. V., Kucharek, H., Möbius, E., Walker, S. N., Balogh, A., Burgess, D., Lembège, B., Lucek, E. A., Scholer, M., Schwartz7 10, S. J., Thomsen, M. F., Bale, S. D., Balikhin, M. A., Balogh, A., Horbury, T. S., Krasnoselskikh, V. V., Kucharek, H., Lembège, B., Möbius, E., Schwartz, S. J., Thomsen, M. F., Walker, S. N., Balogh, A., Burgess, D., Lembège, B., Lucek, E. A., Scholer, M., Schwartz7 10, S. J., Thomsen, M. F., Bale, S. D., Balikhin, M. A., Balogh, A., Horbury, T. S., Krasnoselskikh, V. V., Kucharek, H., Lembège, B., Möbius, E., Schwartz, S. J., Thomsen, M. F., Walker, S. N., Balogh, A., Burgess, D., Lembège, B., Lucek, E. A., Scholer, M., Schwartz7 10, S. J., Thomsen, M. F., Bale, S. D., Balikhin, M. A., Balogh, A., Horbury, T. S., Krasnoselskikh, V. V., Kucharek, H., Lembège, B., Möbius, E., Schwartz, S. J., Thomsen, M. F., and Walker, S. N. (2005). Quasi-perpendicular Shock Structure and Processes. *Space Science Reviews*, 118(1-4):161–203.

Balikhin, M. and Gedalin, M. (1994). Kinematic mechanism of electron heating in shocks: Theory vs observations. *Geophysical Research Letters*, 21(9):841–844.

Balikhin, M., Krasnoselskikh, V. V., and Gedalin, M. (1995). The scales in quasiperpendicular shocks. *Advances in Space Research*, 15(8-9):247–260.

Balikhin, M. A., Zhang, T. L., Gedalin, M., Ganushkina, N. Y., and Pope, S. A. (2008). Venus express observes a new type of shock with pure kinematic relaxation. *Geophysical Research Letters*, 35(1):1–5.

Balogh, A., Dunlop, M. W., Cowley, S. W. H., Southwood, D. J., Thomlinson, J. G., Glassmeier, K. H., Musmann, G., Lühr, H., Buchert, S., Acuña, M. H., Fairfield, D. H., Slavin, J. A., Riedler, W., Schwingenschuh, K., and Kivelson, M. G. (1997). The Cluster Magnetic Field Investigation. In *The Cluster and Phoenix Missions*, pages 65–91. Springer Netherlands, Dordrecht.

Balogh, A. and Riley, P. (1997). Overview of heliospheric shocks. In *Cosmic Winds and the Heliosphere*, page 359. University of Arizona Press.

Barabash, S., Sauvaud, J. A., Gunell, H., Andersson, H., Grigoriev, A., Brinkfeldt, K., Holmstrom, M., Lundin, R., Yamauchi, M., Asamura, K., Baumjohann, W., Zhang, T. L., Coates, A. J., Linder, D. R., Kataria, D. O., Curtis, C. C., Hsieh, K. C., Sandel, B. R., Fedorov, A., Mazelle, C., Thocaven, J. J., Grande, M., Koskinen, H. E. J., Kallio, E., Sales, T., Riihela, P., Kozyra, J., Krupp, N., Woch, J., Luhmann, J., McKenna-Lawlor, S., Orsini, S., Cerulli-Irelli, R., Mura, M., Milillo, M., Maggi, M., Roelof, E., Brandt, P., Russell, C. T., Szego, K., Winningham, J. D., Frahm, R. A., Scherrer, J., Sharber, J. R., Wurz, P., and Bochsler, P. (2007). The Analyser of Space Plasmas and Energetic Atoms (ASPERA-4) for the Venus Express mission. *Planetary and Space Science*, 55(12):1772–1792.

Baumjohann, W. and Treumann, R. (1996). *Basic space plasma physics*.

Baumjohann, W., Treumann, R. A., Georgescu, E., Haerendel, G., Fornacon, K.-H., and Auster, U. (1999). Waveform and packet structure of lion roars. *Annales Geophysicae*, 17(12):1528–1534.

Baumjohann, W., Treumann, R. R. A., and Treumann, R. R. A. (1996). *Basic space plasma physics*, volume 57. World Scientific.

Behlke, R., André, M., Buchert, S. C., Vaivads, A., Eriksson, A. I., Lucek, E. A., and Balogh, A. (2003). Multi-point electric field measurements of Short Large-Amplitude Magnetic Structures (SLAMS) at the earth's quasi-parallel bow shock. *Geophysical Research Letters*, 30(4):1–4.

BELLAN, P. M. (2008). *Fundamentals of Plasma Physics*. Cambridge University Press.

Blandford, R. and Eichler, D. (1987). Particle acceleration at astrophysical shocks: A theory of cosmic ray origin. *Physics Reports*, 154(1):1–75.

Breneman, A., Cattell, C., Schreiner, S., Kersten, K., Wilson, L. B., Kellogg, P., Goetz, K., and Jian, L. K. (2010). Observations of large-amplitude, narrowband whistlers at stream interaction regions. *Journal of Geophysical Research: Space Physics*, 115(8):1–11.

Breuillard, H., Contel, O. L., Chust, T., Berthomier, M., Retino, A., Turner, D. L., Nakamura, R., Baumjohann, W., Cozzani, G., Catapano, F., Alexandrova, A., Mirioni, L., Graham, D. B., Argall, M. R., Fischer, D., Wilder, F. D., Gershman, D. J., Varsani, A., Lindqvist, P.-A., Khotyaintsev, Y. V., Marklund, G., Ergun, R. E., Goodrich, K. A., Ahmadi, N., Burch, J. L., Torbert, R. B., Needell, J., Chutter, M., Rau, D., Dors, I., Russell, C. T., Magnes, W., Strangeway, R. J., Bromund, K. R., Wei, H., Plaschke, F., Anderson, B. J., Le, G., Moore, T. E., Giles, B. L., Paterson, W. R., Pollock, C. J., Dorelli, J. C., Avanov, L. A., Saito, Y., Lavraud, B., Fuselier, S. A., Mauk, B. H., Cohen, I. J., and Fennell, J. F. (2017). The properties of lion roars and electron dynamics in mirror-mode waves observed by the Magnetospheric MultiScale mission. *Journal of Geophysical Research: Space Physics*.

Brice, N. (1964). Fundamentals of very low frequency emission generation mechanisms. *Journal of Geophysical Research*, 69(21):4515–4522.

Burgess, D., Lucek, E. A., Scholer, M., Bale, S. D., Balikhin, M. A., Balogh, A., Horbury, T. S., Krasnoselskikh, V. V., Kucharek, H., Lembège, B., Möbius, E., Schwartz, S. J., Thomsen, M. F., and Walker, S. N. (2005). Quasi-parallel Shock Structure and Processes. *Space Science Reviews*, 118(1-4):205–222.

Chang, O., Gary, S. P., and Wang, J. (2013). Whistler turbulence at variable electron beta: Three-dimensional particle-in-cell simulations. *Journal of Geophysical Research: Space Physics*, 118(6):2824–2833.

Coroniti, F. V. (1970). Dissipation discontinuities in hydromagnetic shock waves. *Journal of Plasma Physics*, 4(02):265–282.

Coroniti, F. V. (1971). Laminar Wave-Train Structure Of Collision Less Magnetic Slow Shocks. *Nuclear Fusion*, 11(3):261–283.

De Hoffmann, F. and Teller, E. (1950). Magneto-hydrodynamic shocks. *Physical Review*, 80(4):692–703.

Décréau, P. M. E., Fergeau, P., Krannosels'kikh, V., Lévêque, M., Martin, P., Randriamboarison, O., Sené, F. X., Trotignon, J. G., Canu, P., and Mögensen, P. B. (1997). WHISPER, A Resonance Sounder and Wave Analyser : Performances and Perspectives for the Cluster Mission. *Space Science Reviews*, 79(1/2):157–193.

Edmiston, J. P. and Kennel, C. F. (1984). A parametric survey of the first critical Mach number for a fast MHD shock. *Journal of Plasma Physics*, 32(03):429.

Edmiston, J. P., Kennel, C. F., and Eichler, D. (1982). Escape of heated ions upstream of quasiparallel shocks. *Geophysical Research Letters*, 9(5):531–534.

Fairfield, D. H. (1969). Bow shock associated waves observed in the far upstream interplanetary medium. *Journal of Geophysical Research*, 74(14):3541–3553.

Fairfield, D. H. (1974). Whistler waves observed upstream from collisionless shocks. *Journal of Geophysical Research*, 79(10):1368–1378.

Farris, M. H., Petrinec, S. M., and Russell, C. T. (1991). The thickness of the magnetosheath: Constraints on the polytropic index. *Geophysical Research Letters*, 18(10):1821–1824.

Farris, M. H. and Russell, C. T. (1994). Determining the standoff distance of the bow shock: Mach number dependence and use of models. *Journal of Geophysical Research*, 99(A9):17681.

Formisano, V. and Kennel, C. F. (1969). Small amplitude waves in high β plasmas. *Journal of Plasma Physics*, 3(01):55.

Gary, S. P. and Mellott, M. M. (1985). Whistler Damping at Oblique Propagation: Laminar Shock Precursors. *Journal of Geophysical Research*, 90(A1):99–104.

Gedalin, M. (1996). Ion reflection at the shock front revisited. *Journal of Geophysical Research: Space Physics*, 101(A3):4871–4878.

Gedalin, M., Gedalin, K., Balikhin, M., and Krasnosselskikh, V. (1995). Demagnetization of electrons in the electromagnetic field structure, typical for quasi-perpendicular collisionless shock front. *Journal of Geophysical Research*, 100(A6):9481.

Giagkiozis, S., Walker, S. N., Pope, S. A., and Collinson, G. A. (2017). Validation of Single Spacecraft Methods for Collisionless Shock Velocity Estimation. *Journal of Geophysical Research: Space Physics*.

Giagkiozis, S., Wilson, L. B., Burch, J. L., Le Contel, O., Ergun, R., Gershman, D. J., Lindqvist, P.-A., Mirioni, L., Moore, T. E., Strangeway, R. J., Contel, O. L., Ergun, R., Gershman, D. J., Lindqvist, P.-A., Mirioni, L., Moore, T. E., and Robert, J. (2018). Statistical Study of the Properties of Magnetosheath Lion Roars. *Journal of Geophysical Research: Space Physics*.

Gosling, J. T. and Thomsen, M. F. (1985). Specularly reflected ions, shock foot thicknesses, and shock velocity determinations in space. *Journal of Geophysical Research*, 90(A10):9893.

Hada, T. (1994). Evolutionary conditions in the dissipative MHD system: Stability of intermediate MHD shock waves. *Geophysical Research Letters*, 21(21):2275–2278.

Hada, T. and Kennel, C. F. (1985). Nonlinear Evolution of Slow Waves in the Solar Wind. *Journal of Geophysical Research*, 90(A1):531–535.

Hill, P., Paschmann, G., Treumann, R. A., Baumjohann, W., Sckopke, N., and Lühr, H. (1995). Plasma and magnetic field behavior across the magnetosheath near local noon. *Journal of Geophysical Research: Space Physics*, 100(A6):9575–9583.

Hoppe, M. M., Russell, C. T., Frank, L. A., Eastman, T. E., and Greenstadt, E. W. (1981). Upstream Hydromagnetic Waves and Their Association with Backstreaming Ion Populations: ISEE 1 and 2 Observations. *Journal of Geophysical Research*, 86(A6):4471–4492.

Hoppe, M. M., Russell, C. T. C., Eastman, T. E., and Frank, L. A. (1982). Characteristics of the ULF Waves Associated with Upstream Ion Beams. *Journal of Geophysical . . .*, 87(A2):643–650.

Horbury, T. S., Cargill, P. J., Lucek, E. A., Balogh, A., Dunlop, M. W., Oddy, T. M., Carr, C., Brown, P., Szabo, A., and Fornaçon, K.-H. (2001). Cluster magnetic field observations of the bowshock: Orientation, motion and structure. *Annales Geophysicae*, 19(10/12):1399–1409.

Hughes, R. S., Gary, S. P., and Wang, J. (2014). Electron and ion heating by whistler turbulence: Three-dimensional particle-in-cell simulations. *Geophysical Research Letters*, 41(24):8681–8687.

Kallenrode, M. (2004). Space Physics: An Introduction to Plasmas and Particles in the Heliosphere and Magnetospheres.

Kantrowitz, A. R. and Petschek, H. E. (1964). MHD characteristics and shock waves. Technical report.

Kennel, C. and Petschek, H. (1966). Limit on stably trapped particle fluxes. *Journal of Geophysical Research*, 71:1–28.

Kennel, C. F., Edmiston, J. P., and Hada, T. (1985). A quarter century of collisionless shock research. In *Collisionless shocks in the heliosphere: Reviews of current research*, pages 1974–1979. American Geophysical Union.

Kivelson, M. G. and Russell, C. T. (1995). *Introduction to space physics*. Cambridge University Press.

Kivelson, M. G. and Southwood, D. J. (1996). Mirror instability II: The mechanism of nonlinear saturation. *Journal of Geophysical Research: Space Physics*, 101(A8):17365–17371.

Krasnoselskikh, V. V. (1985). Nonlinear motions of a plasma across a magnetic field. *Sov. Phys. JETP*, 62(August 1985):282–288.

Krasnoselskikh, V. V., Balikhin, M., Walker, S. N., Schwartz, S., Sundkvist, D., Lobzin, V., Gedalin, M., Bale, S. D., Mozer, F., Soucek, J., Hobara, Y., and Comisel, H. (2013). The dynamic quasiperpendicular shock: Cluster discoveries. *Space Science Reviews*, 178(2-4):535–598.

Krasnoselskikh, V. V., Lembège, B., Savoini, P., and Lobzin, V. V. (2002). Nonstationarity of strong collisionless quasiperpendicular shocks: Theory and full particle numerical simulations. *Physics of Plasmas*, 9(4):1192.

Le Contel, O., Leroy, P., Roux, A., Coillot, C., Alison, D., Bouabdellah, A., Mirioni, L., Meslier, L., Galic, A., Vassal, M. C., Torbert, R. B., Needell, J., Rau, D., Dors, I., Ergun, R. E., Westfall, J., Summers, D., Wallace, J., Magnes, W., Valavanoglou, A., Olsson, G., Chutter, M., Macri, J., Myers, S., Turco, S., Nolin, J., Bodet, D., Rowe, K., Tanguy, M., and de la Porte, B. (2016). The Search-Coil Magnetometer for MMS. *Space Science Reviews*, 199(1-4):257–282.

Lengyel-Frey, D., Farrell, W. M., Stone, R. G., Balogh, A., and Forsyth, R. (1994). An analysis of whistler waves at interplanetary shocks. *Journal of Geophysical Research*, 99(A7):13325.

Leroy, M. M., Winske, D., Goodrich, C. C., Wu, C. S., and Papadopoulos, K. (1982). The structure of perpendicular bow shocks. *Journal of Geophysical Research*, 87(A7):5081.

Li, X., Lewis, H. R., LaBelle, J., Phan, T.-D., and Treumann, R. A. (1995). Characteristics of the ion pressure tensor in the Earth's magnetosheath. *Geophysical Research Letters*, 22(6):667–670.

Livesey, W. A., Kennel, C. F., and Russell, C. T. (1982). ISEE-1 and -2 observations of magnetic field strength overshoots in quasi-perpendicular bow shocks. *Geophysical Research Letters*, 9(9):1037–1040.

Livesey, W. A., Russell, C. T., and Kennel, C. F. (1984). A comparison of specularly reflected gyrating ion orbits with observed shock foot thicknesses. *Journal of Geophysical Research*, 89(A8):6824.

Lobzin, V. V., Krasnoselskikh, V. V., Bosqued, J.-M., Pinçon, J.-L., Schwartz, S. J., and Dunlop, M. (2007). Nonstationarity and reformation of high-Mach-number quasiperpendicular shocks: Cluster observations. *Geophysical Research Letters*, 34(5):2899–2910.

Lucek, E. A., Constantinescu, D., Goldstein, M. L., Pickett, J., Pin??on, J. L., Sahraoui, F., Treumann, R. A., and Walker, S. N. (2005). The magnetosheath. *Space Science Reviews*, 118(1-4):95–152.

Marshall, W. (1955). The Structure of Magneto-Hydrodynamic Shock Waves. *Proceedings of the Royal Society A: Mathematical, Physical and Engineering Sciences*, 233(1194):367–376.

Masood, W., Schwartz, S. J., Maksimovic, M., and Fazakerley, A. N. (2006). Electron velocity distribution and lion roars in the magnetosheath. *Annales Geophysicae*, 24(6):1725–1735.

McComas, D., Alexashov, D., Bzowski, M., Fahr, H., Heerikhuisen, J., Izmodenov, V., Lee, M., M{\"o}bius, E., Pogorelov, N., Schwadron, N., and Zank, G. (2012). The heliosphere's interstellar interaction: No bow shock. *Science*, 336(6086):1291—-1293.

Morse, D. L., Destler, W. W., and Auer, P. L. (1972). Nonstationary Behaviour of Collisionless Shocks. *Physical Review Letters*, 28(1):13–16.

Moses, S. L., Coroniti, F. V., Kennel, C. F., Scarf, F. L., Greenstadt, E. W., Kurth, W. S., and Lepping, R. P. (1985). High time resolution plasma wave and magnetic field observations of the Jovian bow shock. *Geophysical Research Letters*, 12(4):183–186.

Moullard, O., Burgess, D., and Bale, S. D. (1998). Whistler waves observed during an in-situ solar type III radio burst. *Astronomy and Astrophysics*, 335:703–708.

Moullard, O., Burgess, D., Salem, C., Mangeney, A., Larson, D. E., and Bale, S. D. (2001). Whistler waves , Langmuir waves and single loss cone electron distributions inside a magnetic cloud : Observations. *Journal of Geophysical Research*, 106(A5):8301–8313.

Paschmann, G., Sckopke, N., Papamastorakis, I., Asbridge, J. R., Bame, S. J., and Gosling, J. T. (1981). Characteristics of reflected and diffuse ions upstream from the Earth's bow shock. *Journal of Geophysical Research: Space Physics*, 86(A6):4355–4364.

Phan, T. D., Larson, D., Moyer, M., McFadden, J. P., Lin, R. P., Carlson, C. W., McCarthy, M., Parks, G. K., Rème, H., Sanderson, T. R., Lepping, R. P., and Paularena, K. I. (1997). The low-latitude flank magnetosheath, magnetopause and boundary layer: wind observations. *Advances in Space Research*, 20(4):809–812.

Phan, T. D., Larson, D. E., Lin, R. P., McFadden, J. P., Anderson, K. A., Carlson, C. W., Ergun, R. E., Ashford, S. M., McCarthy, M. P., Parks, G. K., Rème, H., Bosqued, J. M., D'Uston, C., Wenzel, K.-P., Sanderson, T. R., and Szabo, A. (1996). The subsolar magnetosheath and magnetopause for high solar wind ram pressure: WIND observations. *Geophysical Research Letters*, 23(10):1279–1282.

Pollock, C., Moore, T., Jacques, A., Burch, J., Gliese, U., Saito, Y., Omoto, T., Avanov, L., Barrie, A., Coffey, V., Dorelli, J., Gershman, D., Giles, B., Rosnack, T., Salo, C., Yokota, S., Adrian, M., Aoustin, C., Auletti, C., Aung, S., Bigio, V., Cao, N., Chandler, M., Chornay, D., Christian, K., Clark, G., Collinson, G., Corris, T., De Los Santos, A., Devlin, R., Diaz, T., Dickerson, T., Dickson, C., Diekmann, A., Diggs, F., Duncan, C., Figueroa-Vinas, A., Firman, C., Freeman, M., Galassi, N., Garcia, K., Goodhart, G., Guererro, D., Hageman, J., Hanley, J., Hemminger, E., Holland, M., Hutchins, M., James, T., Jones, W., Kreisler, S., Kujawski, J., Lavu, V., Lobell, J., LeCompte, E., Lukemire, A., MacDonald, E., Mariano, A., Mukai, T., Narayanan, K., Nguyan, Q., Onizuka, M., Paterson, W., Persyn, S., Piepgrass, B., Cheney, F., Rager, A., Raghuram, T., Ramil, A., Reichenthal, L., Rodriguez, H., Rouzaud, J., Rucker, A., Saito, Y., Samara, M., Sauvaud, J.-A., Schuster, D., Shappirio, M., Shelton, K., Sher, D., Smith, D., Smith, K., Smith, S., Steinfeld, D., Szymkiewicz, R., Tanimoto, K., Taylor, J., Tucker, C., Tull, K., Uhl, A., Vloet, J., Walpole, P., Weidner, S., White, D., Winkert, G., Yeh, P.-S., and Zeuch, M. (2016). Fast Plasma Investigation for Magnetospheric Multiscale. *Space Science Reviews*, 199(1-4):331–406.

Pope, S. A., Zhang, T. L., Balikhin, M. A., Delva, M., Hvizdos, L., Kudela, K., and Dimmock, A. P. (2011). Exploring planetary magnetic environments using magnetically unclean spacecraft: A systems approach to VEX MAG data analysis. *Annales Geophysicae*, 29(4):639–647.

Rème, H., Bosqued, J. M., Sauvaud, J. A., Cros, A., Dandouras, J., Aoustin, C., Bouyssou, J., Camus, T., Cuvilo, J., Martz, C., Médale, J. L., Perrier, H., Romefort, D., Rouzaud, J., D'Uston, C., Möbius, E., Crocker, K., Granoff, M., Kistler, L. M., Popecki, M., Hovestadt, D., Klecker, B., Paschmann, G., Scholer, M., Carlson, C. W., Curtis, D. W., Lin, R. P., McFadden, J. P., Formisano, V., Amata,

E., Bavassano-Cattaneo, M. B., Baldetti, P., Belluci, G., Bruno, R., Chionchio, G., Di Lellis, A., Shelley, E. G., Ghielmetti, A. G., Lennartsson, W., Korth, A., Rosenbauer, H., Lundin, R., Olsen, S., Parks, G. K., McCarthy, M., and Balsiger, H. (1997). The Cluster Ion Spectrometry (CIS) Experiment. In *The Cluster and Phoenix Missions*, pages 303–350. Springer Netherlands, Dordrecht.

Rodriguez, P. (1979). Magnetosheath electrostatic turbulence. *Journal of Geophysical Research*, 84(A3):917.

Russell, C. T., Anderson, B. J., Baumjohann, W., Bromund, K. R., Dearborn, D., Fischer, D., Le, G., Leinweber, H. K., Leneman, D., Magnes, W., Means, J. D., Moldwin, M. B., Nakamura, R., Pierce, D., Plaschke, F., Rowe, K. M., Slavin, J. A., Strangeway, R. J., Torbert, R., Hagen, C., Jernej, I., Valavanoglou, A., and Richter, I. (2016). The Magnetospheric Multiscale Magnetometers. *Space Science Reviews*, 199(1-4):189–256.

Russell, C. T., Childers, D. D., and Coleman Jr., P. J. (1971). Ogo 5 Observations of Upstream Waves in the Interplanetary Medium- Discrete Wave Packets. *Journal of Geophysical . . .*, 76(4):845–861.

Saxena, R., Bale, S. D., and Horbury, T. S. (2005). Wavelength and decay length of density overshoot structure in supercritical, collisionless bow shocks. *Physics of Plasmas*, 12(5):1–6.

Schwartz, S. (1998). Shock and Discontinuity Normals, Mach Numbers, and Related Parameters. *ISSI Scientific Reports Series*, 1:249–270.

Schwartz, S. J. and Burgess, D. (1991). Quasi-parallel shocks: A patchwork of three-dimensional structures. *Geophysical Research Letters*, 18(3):373–376.

Schwartz, S. J., Burgess, D., and Moses, J. J. (1996). Low-frequency waves in the Earth's magnetosheath: present status. *Annales Geophysicae*, 14(11):1134–1150.

Sckopke, N., Gosling, J. T., Russell, C. T., and Bame, S. J. (1983). Evolution of Ion Distributions Across the Nearly Perpendicular Bow Shock: Specularly and Non-Specularly Reflected-Gyrating Ions. *Journal of Geophysical Research*, 88(A8):6121–6136.

Silverman, B. W. (1986). *Density Estimation for Statistics and Data Analysis*, volume 37.

Smith, E. J., Holzer, R. E., and Russell, C. T. (1969). Magnetic emissions in the magnetosheath at frequencies near 100 Hz. *Journal of Geophysical Research*, 74(11):3027–3036.

Smith, E. J. and Tsurutani, B. T. (1976). Magnetosheath Lion Roars. *Journal of Geophysical Research*, 81(13):2261–2266.

Torbert, R. B., Russell, C. T., Magnes, W., Ergun, R. E., Lindqvist, P.-A., LeContel, O., Vaith, H., Macri, J., Myers, S., Rau, D., Needell, J., King, B., Granoff, M., Chutter, M., Dors, I., Olsson, G., Khotyaintsev, Y. V., Eriksson, A., Kletzing, C. A., Bounds, S., Anderson, B., Baumjohann, W., Steller, M., Bromund, K., Le, G., Nakamura, R., Strangeway, R. J., Leinweber, H. K., Tucker, S., Westfall, J., Fischer, D., Plaschke, F., Porter, J., and Lappalainen, K. (2016). The FIELDS Instrument Suite on MMS: Scientific Objectives, Measurements, and Data Products. *Space Science Reviews*, 199(1-4):105–135.

Tsurutani, B. T., Smith, E. J., Anderson, R. R., Ogilvie, K. W., Scudder, J. D., Baker, D. N., and Bame, S. J. (1982). Lion roars and nonoscillatory drift mirror waves in the magnetosheath. *Journal of Geophysical Research*, 87(A8):6060.

Vedenov, A. A. and Sagdeev, R. Z. (1961). Some properties of plasma with an anisotropic ion velocity distribution in a magnetic field. *Plasma Physics and the Problem of Controlled Thermonuclear Reactions*, 3:332–339.

Walker, S. N., Balikhin, M. a., and Nozdrachev, M. N. (1999). Ramp nonstationarity and the generation of whistler waves upstream of a strong quasiperpendicular shock. *Geophysical Research Letters*, 26(10):1357–1360.

Whang, Y. C., Zhou, J., Lepping, R. P., and Ogilvie, K. W. (1996). Interplanetary slow shock observed from Wind. *Geophysical Research Letters*, 23(10):1239–1242.

Wilson, L. B., Koval, A., Szabo, A., Breneman, A., Cattell, C. A., Goetz, K., Kellogg, P. J., Kersten, K., Kasper, J. C., Maruca, B. A., and Pulupa, M. (2013). Electromagnetic waves and electron anisotropies downstream of supercritical interplanetary shocks. *Journal of Geophysical Research: Space Physics*, 118(1):5–16.

Wilson III, L. B., Koval, A., Szabo, A., Stevens, M. L., Kasper, J. C., Cattell, C. A., and Krasnoselskikh, V. V. (2017). Revisiting the structure of low-Mach number, low-beta, quasi-perpendicular shocks. *Journal of Geophysical Research: Space Physics*, pages 1–19.

Woods, L. (1969). On the structure of collisionless magneto-plasma shock waves at super-critical Alfvén-Mach numbers. *Journal of Plasma Physics*, 3:435–447.

Woods, L. C. (1971). On double-structured, perpendicular, magneto-plasma shock waves. *Plasma Physics*, 13(4):289–302.

Wu, C. C. (1987). On MHD intermediate shocks. *Geophysical Research Letters*, 14(6):668–671.

Wu, C. C. and Hada, T. (1991). Formation of intermediate shocks in both two-fluid and hybrid models. *Journal of Geophysical Research*, 96(A3):3769.

Zhang, T. L., Baumjohann, W., Delva, M., Auster, H. U., Balogh, A., Russell, C. T., Barabash, S., Balikhin, M., Berghofer, G., Biernat, H. K., Lammer, H., Lichtenegger, H., Magnes, W., Nakamura, R., Penz, T., Schwingenschuh, K., Vörös, Z., Zambelli, W., Fornacon, K. H., Glassmeier, K. H., Richter, I., Carr, C., Kudela, K., Shi, J. K., Zhao, H., Motschmann, U., and Lebreton, J. P. (2006). Magnetic field investigation of the Venus plasma environment: Expected new results from Venus Express. *Planetary and Space Science*, 54(13-14):1336–1343.

Zhang, T. L., Berghofer, G., Magnes, W., Delva, M., Baumjohann, W., Biernat, H., Lichtenegger, R., Nakamura, R., Schwingenschuh, K., Auster, H. U., Fornacon, K. H., Richter, I., Glassmeier, K. H., Carr, C., Balogh, A., Barabash, S., Kudela, K., Balikhin, M. A., Russell, C. T., Motschmann, U., and Lebreton, J. P. (2005). The fluxgate magnetometer for the Venus Express Mission.

Zhang, Y., Matsumoto, H., and Kojima, H. (1998). Lion roars in the magnetosheath: The Geotail observations. *Journal of Geophysical Research: Space Physics*, 103(A3):4615–4626.